Bernstein modes in a non-neutral plasma column

Daniel Walsh and Daniel H. E. Dubin
Department of Physics, UCSD, La Jolla, California 92093, USA

(Received 6 March 2018; accepted 18 April 2018; published online 23 May 2018)

This paper presents theory and numerical calculations of electrostatic Bernstein modes in an inhomogeneous cylindrical plasma column. These modes rely on finite Larmor radius effects to propagate radially across the column until they are reflected when their frequency matches the upper hybrid frequency. This reflection sets up an internal normal mode on the column and also mode-couples to the electrostatic surface cyclotron wave (which allows the normal mode to be excited and observed using external electrodes). Numerical results predicting the mode spectra, using a novel linear Vlasov code on a cylindrical grid, are presented and compared to an analytical Wentzel Kramers Brillouin (WKB) theory. A previous version of the theory [D. H. E. Dubin, Phys. Plasmas **20**(4), 042120 (2013)] expanded the plasma response in powers of 1/B, approximating the local upper hybrid frequency, and consequently, its frequency predictions are spuriously shifted with respect to the numerical results presented here. A new version of the WKB theory avoids this approximation using the exact cold fluid plasma response and does a better job of reproducing the numerical frequency spectrum. The effect of multiple ion species on the mode spectrum is also considered, to make contact with experiments that observe cyclotron modes in a multi-species pure ion plasma [M. Affolter *et al.*, Phys. Plasmas **22**(5), 055701 (2015)]. *Published by AIP Publishing.*
https://doi.org/10.1063/1.5027848

I. INTRODUCTION

This paper presents a linearized theory of electrostatic cyclotron waves in both single and multiple-species nonneutral plasma columns. For simplicity, we consider the component of plasma response independent of axial position z, but we include thermal effects on the waves, focussing mainly on Bernstein modes. There have been several experimental[2–4] and theoretical[1,5,6] papers studying electrostatic cyclotron waves in a nonneutral plasma in the cold-fluid regime (neglecting thermal effects). In seminal work that included thermal effects, Gould and LaPointe[4] treated a parabolic-profile plasma using an approximate wave equation to estimate Bernstein mode frequencies and also performed experiments that observed the modes on a pure electron plasma column. A partial Wentzel Kramers Brillouin (WKB) theory analysis was provided, but it neglected mode-coupling between the Bernstein and surface cyclotron modes. While Bernstein modes were observed in these experiments, the plasma was not well characterized, as parameters of the plasma (radius, temperature, etc.) were time-dependent as the plasma decayed toward the wall.

In 1995, Sarid *et al.*[3] measured cyclotron modes in a magnesium ion plasma with multiple species. Multiple modes were observed near the ion cyclotron frequency, some of which may have been Bernstein modes, but the plasma was not sufficiently well-characterized to determine this. Recently, Hart and Spencer performed particle-in-cell simulations on an infinite-length plasma in global thermal equilibrium[6] and observed azimuthally symmetric Bernstein modes. Meanwhile, Dubin carried out a full WKB warm fluid theory describing Bernstein modes, extending the work of Gould by accounting for accurate equilibrium distributions and retaining the crucial linear mode coupling between the internal Bernstein and surface cyclotron modes.[1] However, a large magnetic field limit was assumed by Dubin and it is *a priori* unclear how large the magnetic field must be for this approximation to be valid.

In this paper, we present a novel computational method for solution of the linearized Vlasov equation that makes no assumptions about the magnetic field strength and makes direct comparison to previous work by Dubin, and Hart and Spencer. Using the numerical Bernstein spectrum obtained from the code, we find that the 1/B expansion used by Dubin introduces a spurious shift of the local upper-hybrid frequency, leading to a significant shift of Dubin's predicted Bernstein mode frequencies away from the values obtained from our code. We resolve this issue by constructing a *new WKB theory*, which avoids taking the large magnetic field limit. The results of the Vlasov code and the new WKB theory are then compared and better agreement is found between the mode frequencies obtained from the two methods. We also consider the effect of multiple species on the Bernstein mode spectrum, finding that wave-particle resonances (WPR) will damp the waves if the impurity species concentrations are too large. We predict that for ongoing experiments at UCSD, where the modes are excited using applied oscillatory voltages on external electrodes, Bernstein modes will be easiest to observe in the majority species of a clean, hot plasma for azimuthal mode number $l = 2$. For $l = 1$, there is a negligible Bernstein mode response to this type of excitation, and for $l = 0$, the Bernstein mode component to the plasma response is small and heavily damped. However, the $\ell = 0$ Bernstein frequencies predicted by our computations are the same as the results of Hart and Spencer.[6]

II. EQUILIBRIUM

In this paper, we assume throughout that the equilibrium plasma is a thermal equilibrium nonneutral plasma with

uniform temperature T and uniform rotation frequency ω_r. We assume that the plasma consists of charge species all with positive charge q, in a uniform magnetic field in the $-z$ direction of strength B. This choice of magnetic field direction implies that the plasma rotates in the positive θ direction (i.e., $\omega_r > 0$) and cyclotron motion is also a rotation in the positive θ direction with cyclotron frequency $\Omega = qB/(mc) > 0$. (If the plasma consists instead of negative charge species, the results in this paper can be applied by assuming a magnetic field in the $+z$ direction.)

We will use nondimensionalized variables. Times are scaled by the central plasma frequency $\omega_p(r=0) = \sqrt{4\pi q^2 n(0)/m}$ associated with one plasma species of mass m and charge q, and lengths are scaled to the central Debye length $\lambda_D(r=0) = \sqrt{T/(4\pi q^2 n(0))}$ where here (and here alone) $n(r)$ is the unscaled plasma number density of the given species. Everywhere else, densities are scaled by the central equilibrium density $n(0)$. Masses of other species are scaled to the mass m. Electric potentials are also scaled via $\Phi = q\phi/T$, where ϕ is the unscaled electrostatic potential. This definition of Φ, along with the scaling of n, gives, for a single-species plasma, the scaled Poisson's Equation $\nabla^2\Phi = -n$. These scalings imply that the velocities are scaled by the thermal speed $v_T = \sqrt{T/m}$.

The thermal equilibrium density profile of the plasma satisfies Poisson's equation with the constraint that $n(r)$ is a Boltzmann distribution. For a single species plasma, we write

$$n(r) = e^{\psi(r)}, \tag{1}$$

where $\psi = -\Phi - \omega_r(\Omega - \omega_r)r^2/2$ is the negative of the (scaled) equilibrium potential energy as seen in a frame rotating with the plasma.[7] Then, the Poisson's equation reduces to

$$\frac{1}{r}\frac{\partial}{\partial r}\left[r\frac{\partial \psi}{\partial r}\right] = e^{\psi} - (1+\gamma), \tag{2}$$

where $\gamma \equiv 2\omega_r(\Omega - \omega_r) - 1$. Densities predicted by Eqs. (1) and (2) are displayed in Fig. 1 for a set of different γ values. As γ approaches zero, the plasma radius (measured in Debye lengths) increases.

In later work, we will find it useful to define the equilibrium radius of the plasma r_p as

$$r_p = \sqrt{\int_0^{r_w} 2rn(r)\,dr}. \tag{3}$$

This radius is equal to the radius of an imaginary "top-hat" plasma whose central density and total particle number (per unit axial length) are both equal to our plasma. In scaled units, there is a relationship between γ and r_p, good when $r_p \gg 1$:

$$r_p \sim 0.513 - \log\gamma + \frac{1}{2}\log\,\log 1/\gamma.$$

Consequently, γ parametrizes the scaled radius of the plasma, i.e., the number of Debye lengths across the column radius.

The equilibrium distribution function is a product of $n(r)$ and a rotating Maxwellian, which in our scaled units becomes

$$f_0(r,\mathbf{v}) = \frac{n(r)}{2\pi} \times \exp\left[-\frac{(\mathbf{v} - \omega_r r\hat{\theta})^2}{2}\right]. \tag{4}$$

For nonneutral plasmas containing multiple species, species with different masses can centrifugally separate in the rotating plasma column, with heavier species pushed to the outside of the column by centrifugal force effects. According to the Boltzmann distribution, the ratio of densities between two species i and j is[8]

$$n_i(r)/n_j(r) = c_{i,j}\exp\left(-(m_i - m_j)\omega_r^2 r^2/2\right), \tag{5}$$

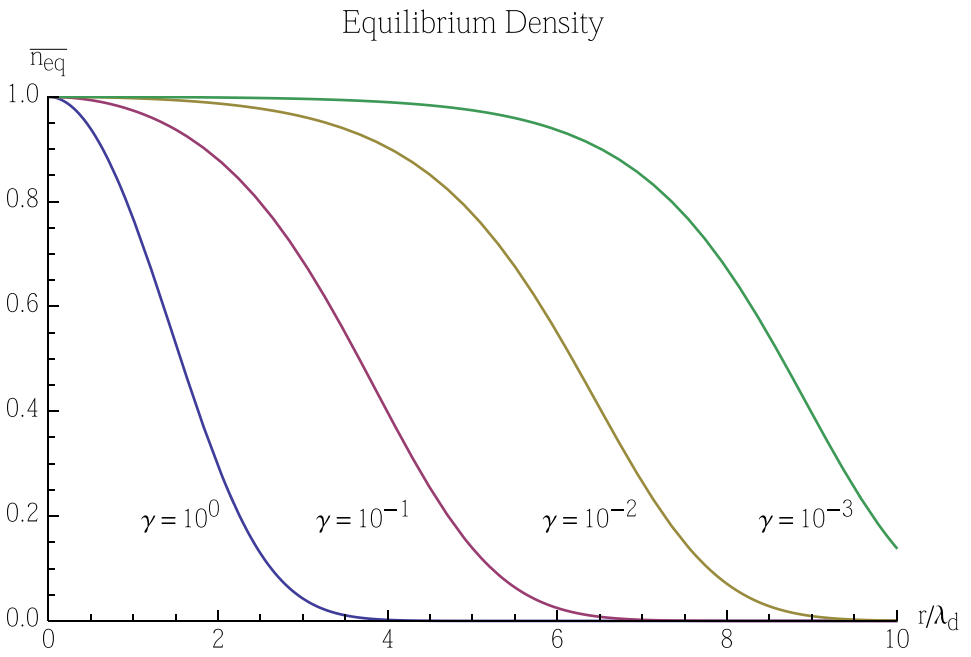

FIG. 1. Equilibrium densities scaled by central density for various values of γ.

where $c_{i,j}$ is a constant depending on the overall concentration of the two species. Here, however, we will assume that the density ratio is close enough to a constant over the plasma profile so that centrifugal separation effects can be neglected. This is not a good approximation in some very low temperature experiments ($T < 10^{-4}$ eV) on ion plasmas at UCSD, but is a reasonably good approximation at higher temperatures where, as we will see, it is easier to see Bernstein modes. Thus, we will assume that each species has the same radial density profile, multiplied by a factor proportional to the overall concentration of that species.

III. COLD FLUID THEORY OF CYCLOTRON WAVES

In this section, we briefly review the general theory of cold fluid electrostatic waves in a plasma column. Readers interested in more details should refer to the original work of Trivelpiece and Gould,[9] as well as a more recent cold fluid theory of z-independent cyclotron waves developed by Gould.[4,5] Temperature is assumed to be zero in this theory and the plasma equilibrium density is assumed to have an arbitrary radial dependence $n(r)$. The theory considers cyclotron waves that are excited by oscillating an external electrode voltage at frequency ω. The electrode radius is $r = r_W$ and its voltage is oscillated to produce a potential on the electrode of the form $\delta\Phi_W e^{-i\omega t + i\ell\theta}$, where ℓ is an integer. For a single-species plasma, Gould derived a linear fluid theory for small amplitude waves, where the perturbed potential $\delta\Phi(r,\theta,t)$ is also proportional to $e^{-i\omega t+i\ell\theta}$ and satisfies the following boundary-value problem:

$$\nabla \cdot \epsilon \nabla \delta\Phi = 0, \tag{6}$$

with a 2-dimensional dielectric tensor ϵ given by

$$\epsilon = \mathbb{1} - \begin{bmatrix} 1 & \dfrac{-i\Omega_v}{\hat{\omega}} \\ \dfrac{i\Omega_v}{\hat{\omega}} & 1 + \dfrac{r\omega_f'\Omega_v}{\hat{\omega}^2} \end{bmatrix} X(\omega, r). \tag{7}$$

Here

$$X(\omega, r) = \frac{\omega_p^2}{\hat{\omega}^2 - \Omega_v(\Omega_v - r\omega_f')}, \tag{8}$$

where we have momentarily relaxed our scaled units, so that the dependence of X on the plasma frequency ω_p is apparent (in our scaled units $\omega_p^2 = n(r)$). The primes denote derivatives with respect to r, $\hat{\omega} = \omega - \ell\omega_f$ is the Doppler-shifted wave frequency as seen in a frame rotating with the plasma, $\Omega_v = \Omega - 2\omega_f$ is the "vortex frequency" (the cyclotron frequency shifted by the Coriolis force from rotation), and $\omega_f(r)$ is the cold-fluid rotation rate of the plasma (neglecting the thermal diamagnetic drift correction that affects ω_r), which is given by the solution of the quadratic equation

$$2\omega_f(\Omega - \omega_f) = \langle n \rangle_r. \tag{9}$$

Here, $\langle n \rangle_r$ is the average equilibrium density within radius r given by

$$\langle n \rangle_r = \frac{2}{r^2}\int_0^r \bar{r} d\bar{r} n(\bar{r}). \tag{10}$$

Equation (6) is merely a restatement of the Maxwell's equation $\nabla \cdot \mathbf{D} = 0$, where the electric displacement vector is $\mathbf{D} = -\epsilon \cdot \nabla\delta\Phi$.

Writing out Eq. (6), one obtains the following second order differential equation that must be solved for the wave potential $\delta\Phi$:

$$0 = \epsilon_{11}\delta\Phi'' + \left(\frac{\epsilon_{11}}{r} + \epsilon_{11}'\right)\delta\Phi' + \left(\frac{i\ell}{r}\epsilon_{12}' - \frac{\ell^2}{r^2}\epsilon_{22}\right)\delta\Phi, \tag{11}$$

where again primes denote derivatives with respect to r. Here, ϵ_{ij} refers to the i,jth component of the dielectric tensor. This equation is to be solved using the boundary conditions that at $r = 0$ the potential must remain finite, and at the surrounding electrode with radius $r = r_W$ the potential is $\delta\Phi(r_W) = \delta\Phi_W$.

Gould made further progress in obtaining the solution of Eq. (11) by taking a large magnetic field limit in order to simplify several terms. We will not use this approximation here because it introduces small but important errors in the solution. Instead, we solve Eq. (11) numerically. However, we will later find it useful to compare to the large field solution, so for completeness we provide the solution below. The general solution to the large-field ordinary differential equation (ODE) can be written analytically as a linear combination of two independent solutions:

$$\delta\Phi = Ar^{-\ell}\int^r d\bar{r}\frac{\bar{r}^{(2\ell-1)}}{D(\bar{r})} + Br^{-\ell}, \tag{12}$$

where $D(r)$ is the large-field form for ϵ_{11},

$$D = 1 - \frac{\omega_p^2/(2\Omega)}{\hat{\omega} - \Omega_v + r\omega_f'/2}, \tag{13}$$

and where the coefficients A and B are determined by the boundary conditions on the solution.[1]

For the simplest possible case of a uniform plasma completely filling the electrode volume out to $r = r_W$, Eq. (11) simply becomes $\epsilon_{11}\nabla^2\delta\Phi = 0$. This implies that either the potential satisfies Laplace's equation, so that there is no density perturbation (and no cyclotron wave) or else $\epsilon_{11} = 0$, which is the dispersion relation for upper hybrid waves in the uniform plasma column. The frequency of these waves (as seen in the rotating frame) is the upper hybrid frequency, given by

$$\hat{\omega}^2 = \omega_p^2 + \Omega_v^2. \tag{14}$$

In a uniform plasma, these upper hybrid oscillations can have any functional form, i.e., $\nabla^2\delta\Phi$ is not determined in cold fluid theory.

Another case that can be handled analytically is a uniform plasma column with radius r_p less than r_W. In this case, there are surface waves in addition to the upper hybrid waves. The surface waves can be excited by the external electrode potential oscillation, i.e., they are driven to large amplitude if the external electrode potential oscillates at the

surface wave frequency. The surface waves themselves have a potential of the form $\delta\Phi \propto r^\ell$ inside the plasma and a frequency given by the solution of the equation

$$\ell(\epsilon_{11} + i\epsilon_{12}) = -\ell\frac{1 + (r_p/r_W)^{2\ell}}{1 - (r_p/r_W)^{2\ell}}. \tag{15}$$

This equation yields a quadratic equation for the wave frequency whose solution is

$$\hat{\omega} = \frac{\Omega_v}{2} \pm \sqrt{\frac{\Omega^2}{4} - \frac{\omega_p^2}{2}\left(\frac{r_p}{r_W}\right)^{2\ell}}. \tag{16}$$

The upper sign yields the frequency of the surface cyclotron wave, while the lower sign yields the frequency of the diocotron wave. When the magnetic field is large, the surface cyclotron frequency can be approximated as

$$\hat{\omega} = \Omega_v + \frac{\omega_p^2}{2\Omega_v}\left[1 - \left(\frac{r_p}{r_W}\right)^{2\ell}\right]. \tag{17}$$

This surface mode frequency is greater than the vortex frequency but less than the upper hybrid frequency.

Both cyclotron and diocotron waves are incompressible distortions of the shape of the plasma column that rotate in θ with angular phase velocity given by $\hat{\omega}/\ell$, as seen in the frame of the plasma's rotation. These surface waves have finite multipole moments, which is why they can create a potential outside of the plasma that can be detected on the wall. For instance, for $\ell = 1$ the plasma center is shifted off-axis and rotates about the center of the trap at the wave phase velocity, while for $\ell = 2$ the plasma distorts into a uniform-density ellipse whose shape rotates about its center.

On the other hand, upper hybrid oscillations in the uniform plasma column cannot be detected, or excited, using wall potentials. For instance, an $\ell = 0$ upper hybrid oscillation corresponds to *any* cylindrically symmetric radial velocity perturbation; such a perturbation will oscillate at the upper hybrid frequency of the column. This perturbation obviously conserves total charge, and therefore, by Gauss' law, creates no field outside the plasma that can be used to detect or excite the mode.

Similarly, upper hybrid oscillations internal to the plasma column can be found with any azimuthal mode number ℓ and (almost) arbitrary radial dependence (again assuming that the plasma column has uniform density). For instance, any initial $\ell = 1$ density perturbation of the form $\delta n(r)e^{i\theta}$, chosen so as not to change the center of mass location of the plasma (i.e., $\int_0^{r_p} d\bar{r}\bar{r}^2\delta n(\bar{r}) = 0$), will not create an $\ell = 1$ (dipole) moment and will therefore be unobservable from outside the plasma. This initial perturbation can then evolve in two ways, depending on the self-consistent initial velocity field. That part of the field which is curl-free evolves as an upper hybrid oscillation; that part which is divergence-free has zero frequency (as seen in the plasma's rotating frame). Although not the subject of this paper, the zero-frequency modes are "convective cell" vortical motions that do not change the perturbed plasma density, by construction. There are an uncountable infinity of such degenerate upper hybrid oscillations and zero-frequency convective cells, but only two surface modes (the diocotron and upper-hybrid branches). Only the surface modes are detectable, or excitable, from the wall.

For a nonuniform plasma column with density that smoothly approaches zero at some radius less than r_W, the surface mode and the continuum of upper hybrid oscillations now couple in an interesting (and nontrivial) way. (Something similar can happen with the diocotron surface mode and the zero-frequency modes.[10]) As the plasma density varies, the upper hybrid frequency varies and the spectrum of upper hybrid oscillations becomes a continuum that spans the range from the vortex frequency (where the density approaches zero) to the central upper hybrid frequency. This continuum includes the surface plasma frequency, and consequently, the formerly discrete surface plasma eigenmode becomes a "quasimode";[10] i.e., it is no longer an undamped eigenmode of the system. However, there remains a damped plasma response to an external driver that consists of a phase-mixed potential response from the upper hybrid continuum, peaked around the former surface plasma frequency. This is a well-known form of spatial Landau-damping that has been discussed previously for other types of plasma waves, such as Langmuir waves[11] and Trivelpiece-Gould modes.[12] (Sidenote: $\ell = 0$ and $\ell = 1$ are exceptional cases. For $\ell = 0$, there is no surface plasma mode, and there is still no coupling between an external wall potential and the upper hybrid continuum (see Sec. VIII D), while for $\ell = 1$ the surface mode remains a discrete "center of mass" eigenmode, even for a nonuniform column.)

To describe the driven response of a nonuniform plasma column at frequencies near the cyclotron frequency, one must now solve Eq. (11) numerically in general (except for the $\ell = 0$ case, which can be calculated analytically, as we discuss later). However, notice that Eq. (11) has regular singular points for radii where ϵ_{11} vanishes, causing $\delta\Phi$ to diverge. This occurs when

$$X(\omega, r) = 1. \tag{18}$$

Note that this is the same condition we had when considering modes in a uniform plasma, resulting in upper-hybrid oscillations in Eq. (14). Accordingly, we define $r_{\mathrm{UH}}(\omega)$ to be a root of Eq. (18), which we refer to as an *upper-hybrid radius*.

For a single species plasma with a thermal equilibrium density profile, one can show that there is at most one solution to Eq. (18), $r = r_{\mathrm{UH}}(\omega)$. However, for multispecies plasmas, there can be more than one solution.

To understand the nature of the fluid theory divergences near an upper-hybrid radius, we perform asymptotic analysis in Eq. (11) near $r_{\mathrm{UH}}(\omega)$ in the case where terms of any order in $\frac{1}{r}$ are neglected. Dropping all such terms in Eq. (11), we obtain

$$\delta\Phi'' + \frac{\epsilon_{11}'}{\epsilon_{11}}\delta\Phi' = 0. \tag{19}$$

Under typical conditions, the root in Eq. (18) is first-order, that is, $X'(\omega, r_{\rm UH}) \neq 0$, so it is viable to expand $\epsilon_{11}(r)$ around $r_{\rm UH}$. We write

$$\epsilon_{11} \sim \frac{1}{\mathcal{L}}(r - r_{\rm UH}), \tag{20}$$

with $\mathcal{L} \equiv 1/\epsilon'_{11}(r_{\rm UH})$, so that Eq. (19) becomes

$$\delta\Phi'' + \frac{1}{r - r_{\rm UH}}\delta\Phi' = 0. \tag{21}$$

The order of the equation can be reduced, and the equation can be directly integrated

$$\delta\Phi'(r) = \frac{A}{r - r_{\rm UH}}. \tag{22}$$

We should emphasize that Eq. (22) is only correct for r near $r_{\rm UH}$ and should be regarded as the first term in a series expansion of $\delta\Phi'$ about the point $r_{\rm UH}$. The next-order terms in the expansion are proportional to $\log(r/r_{\rm UH} - 1)$, a constant of order unity, and so on.

We would like to integrate this expression to obtain $\delta\Phi(r)$. However, the divergence at $r = r_{\rm UH}$ requires careful consideration of the physics: in any physical plasma there will be a small effect from particle collisions, causing waves to damp. Later in the paper, we introduce a simple Krooks model of collisions. This model has the effect of replacing the frequency ω by $\omega + i\nu$ in Eqs. (6)–(18), where ν is the collision rate. This in turn implies that $r_{\rm UH}$, the root of the modified Eq. (18), $X(\omega + i\nu, r) = 1$, is complex. For small ν, a Taylor expansion of this equation implies that the imaginary part of $r_{\rm UH}$ is

$$Im(r_{\rm UH}) = -\nu\frac{\partial X/\partial\omega}{\partial X/\partial r}\bigg|_{r_{\rm UH0}} = \nu\frac{\partial r_{\rm UH0}}{\partial\omega} = -\frac{2\hat{\omega}\nu}{\omega_p^2\partial\epsilon_{11}/\partial r} \equiv \Delta r, \tag{23}$$

where $r_{\rm UH0}$ and Δr are the real and imaginary parts of the upper hybrid radius, respectively

$$r_{\rm UH} = r_{\rm UH0} + i\Delta r, \tag{24}$$

and the last form for Δr in Eq. (23) follows by substitution for X from Eqs. (7), (8), and (18). The sign of Δr can be either positive or negative depending on the sign of the radial gradient of ϵ_{11}. The effect of this in integrating Eq. (22) is to move the pole at $r_{\rm UH}$ slightly away from the real r axis, allowing integration around the pole

$$\delta\Phi(r) = A\log\left(\frac{r_{\rm UH} - r}{r_{\rm UH} - r_0}\right) + \delta\Phi(r_0), \tag{25}$$

where r_0 is a radius below the cutoff radius, and both r and r_0 are close enough to the upper hybrid radius to make Eq. (20) as good approximation. The coefficient A is given here by matching to the derivative of the potential using Eq. (22)

$$A = -\delta\Phi'(r_0)(r_{\rm UH} - r_0). \tag{26}$$

The logarithmic divergence of the perturbed potential near the upper hybrid radius can be seen in Fig. 2 for several different scaled frequencies λ,[5] where

$$\lambda = \frac{\omega - \Omega}{\omega_E}, \tag{27}$$

and where $\omega_E \equiv 1/(2\Omega)$ is the $E \times B$ equilibrium rotation rate at the center of the plasma column (in our dimensionless units). (This frequency scaling is useful because the plasma response to the forcing is largest for frequencies ω for which λ is of order unity. The fluid rotation rate ω_f, given by Eq. (9), differs from ω_E at the column center in that it includes the $F \times B$ drift from centrifugal force effects, but this difference is typically small.) As shown in Fig. 2, the logarithmic divergence changes with radius as λ varies because the upper hybrid radius is a function of frequency through Eq. (18).

The potential picks up an imaginary part, as shown in Fig. 2, even for small ν because, for $r > r_{\rm UH0}$, the real part of the argument of the logarithm in Eq. (25) changes sign

$$\delta\Phi(r) = A\log\left(\frac{r - r_{\rm UH}}{r_{\rm UH} - r_0}\right) + \delta\Phi(r_0) + i\pi A\,\mathrm{Sign}(\Delta r). \tag{28}$$

To determine a resonant surface mode frequency using these results, we consider a dimensionless measure of the plasma response Y, the admittance function, defined as

$$Y = \frac{r_W\dfrac{\partial\delta\Phi}{\partial r}}{\delta\Phi}\bigg|_{r=r_W}. \tag{29}$$

Notice that a cylinder containing no plasma is a simple capacitor, which has purely imaginary experimental admittance (the ratio of current to voltage). Consequently, our theoretical definition of Y for a vacant cylinder will be purely real (the surface charge on the electrode, proportional to $\partial\delta\Phi/\partial r|_{r_W}$, is the time integral of the current). We conclude that the imaginary part of Y is due to the presence of plasma, so for the remainder of this paper we will focus on $\mathrm{Im}(Y)$. For the potential data in Fig. 2, the admittance function is plotted in Fig. 3. These data show a broad peak, caused by

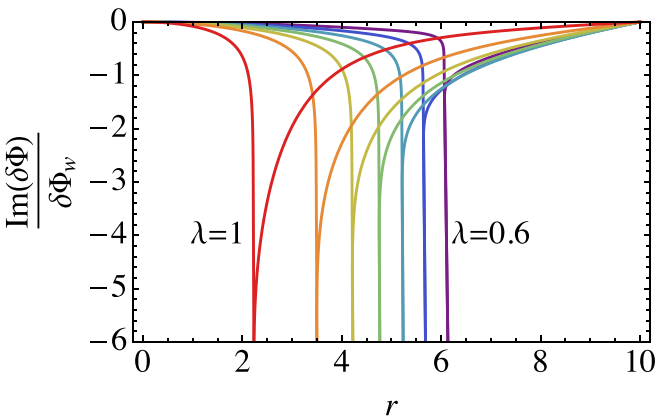

FIG. 2. Radial dependence of the imaginary part of the perturbed potential $\mathrm{Im}\{\delta\Phi(r)\}$ driven at frequencies from $\lambda = 1$ (red) down to $\lambda = 0.6$ (violet) in equal steps. $r_p = 4.76$, $r_W = 10$, $\ell = 2$, $\Omega = 5$, and $\nu \to 0^+$.

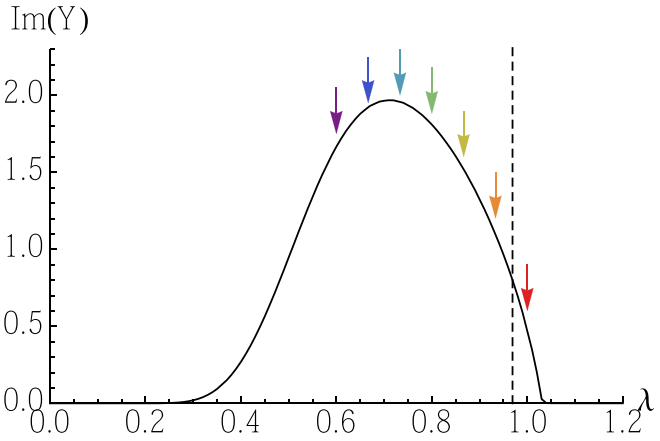

FIG. 3. A plot of $\mathrm{Im}(Y)$ driven at various frequencies, for the plasma parameters of Fig. 2. The colored arrows correspond to the potentials shown in Fig. 2. The dashed line is discussed in the text.

the mixing of the continuum of upper hybrid oscillations and the surface mode, turning the surface mode into a damped quasimode. The width in this peak decreases as the plasma edge becomes sharper (i.e., as temperature decreases holding the plasma radius fixed), approaching a delta function at the surface cyclotron wave frequency given by Eq. (16) (the dashed line), when the plasma density approaches a step function.[1]

IV. VLASOV SOLUTION

So far, the theory has neglected thermal effects responsible for Bernstein modes. In this section, we will develop a numerical approach that keeps these thermal effects. At low temperatures, the method predicts admittance functions that approach the cold-fluid theory, but at higher temperatures Bernstein modes appear as separated peaks in the admittance.

We will develop a numerical method for solution of the linearized Vlasov equation in cylindrical coordinates. In cylindrical coordinates, the Vlasov equation for the distribution function $f(r,\theta,v_r,v_\theta,t)$ is

$$\frac{\partial f}{\partial t}+v_r\frac{\partial f}{\partial r}+\frac{v_\theta}{r}\left(\frac{\partial f}{\partial\theta}-v_r\frac{\partial f}{\partial v_\theta}+v_\theta\frac{\partial f}{\partial v_r}\right)+(-\Omega v_\theta+E_r)\frac{\partial f}{\partial v_r}+(\Omega v_r+E_\theta)\frac{\partial f}{\partial v_\theta}=0, \tag{30}$$

with boundary condition at $r=0$ given by

$$\left.\frac{\partial f}{\partial\theta}-v_r\frac{\partial f}{\partial v_\theta}+v_\theta\frac{\partial f}{\partial v_r}\right|_{r=0}=0,$$

and $f\to 0$ as $r\to\infty$ and when $|\mathbf{v}|\to\infty$. The condition at $r=0$ keeps the third term in Eq. (30) from diverging and physically enforces continuity in f. We will study linear perturbations away from the thermal equilibrium discussed in Sec. I. First, we will change velocity coordinates via $v=\sqrt{v_r^2+v_\theta^2}$, $\tan\psi=\frac{v_\theta}{v_r}$, where v is the magnitude of the velocity, and ψ is the *gyroangle*, or the angle of the velocity relative to the radial direction $\hat{r}$. This gives

$$0=\frac{\partial f}{\partial t}+v\cos\psi\frac{\partial f}{\partial r}+\frac{v\sin\psi}{r}\left(\frac{\partial f}{\partial\theta}-\frac{\partial f}{\partial\psi}\right)+\Omega\frac{\partial f}{\partial\psi}+(E_r\cos\psi+E_\theta\sin\psi)\frac{yf}{\partial v}+\left(\frac{-E_r\sin\psi+E_\theta\cos\psi}{v}\right)\frac{\partial f}{\partial\psi}. \tag{31}$$

In this form, the boundary conditions simplify to

$$\frac{\partial f}{\partial\theta}-\frac{\partial f}{\partial\psi}=0,\quad r=0;\qquad \frac{\partial f}{\partial\psi}=0,\quad v=0;\qquad f\to 0,\ r,v\to\infty. \tag{32}$$

Next, we linearize the equation in the usual way: $f=f_0+\delta f$, where f_0 is a time-independent solution to the non-linear equation. Since the electric potential is determined by both the external wall potential and the charge density in the plasma itself, the electric potential is also expanded as $\phi=\Phi_0+\delta\Phi$ and similarly for the electric field: $\mathbf{E}=\mathbf{E}_0+\delta\mathbf{E}$. The equilibrium plasma density is azimuthally symmetric, so we also use $E_{\theta_0}=0$. Self-consistent magnetic effects are neglected in this treatment, so we omit the $\delta\Omega$ term. Here, we will take f_0 to be the thermal equilibrium solution Eq. (4) solved in Sec. I.

$$0=\frac{\partial\delta f}{\partial t}+v\cos\psi\frac{\partial\delta f}{\partial r}+\frac{v\sin\psi}{r}\left(\frac{\partial\delta f}{\partial\theta}-\frac{\partial\delta f}{\partial\psi}\right)+\Omega\frac{\partial\delta f}{\partial\psi}+E_{r0}\left(\cos\psi\frac{\partial\delta f}{\partial v}-\frac{\sin\psi}{v}\frac{\partial\delta f}{\partial\psi}\right)+(\delta E_r\cos\psi+\delta E_\theta\sin\psi)\frac{\partial f_0}{\partial v}+\left(\frac{-\delta E_r\sin\psi+\delta E_\theta\cos\psi}{v}\right)\frac{\partial f_0}{\partial\psi}. \tag{33}$$

The last term involving a ψ derivative is cumbersome. To remove it, we transform into the co-rotating frame with angular frequency ω_r. This affects the transformation $\Omega\to\Omega_v$, $E_{r_0}\to E_{r_0}+\omega_r(\omega_r-\Omega)r\equiv F_{r_0}$. In these coordinates, $\frac{\partial f_0}{\partial\psi}=0$ (i.e., where $\tan\psi=\bar{v}_\theta/v_r$, with $\bar{v}_\theta$ measured in the rotating frame), eliminating the last term in Eq. (33). Future appearances of v_θ will be understood to be measured in the rotating frame.

We next Fourier analyze in ψ, θ, and t, via

$$\delta f(r,\theta,v_r,v_\theta;t)=e^{-i\omega t+i\ell\theta}\sum_{n=-\infty}^{\infty}\delta f_n(r,v)\,e^{in\psi},\qquad \delta\Phi(r,\theta;t)=\delta\Phi(r)e^{-i\omega t+i\ell\theta}, \tag{34}$$

where we refer to n as the *gyroharmonic number*. Finally, at this point we introduce a Krooks collision term to introduce damping into the system, by adding a term $\nu\,\delta f_n$, driving the plasma back to equilibrium. This has the effect of broadening the frequency response, allowing comparison to experiment and making discrete Bernstein modes visible numerically. The resulting equation becomes

$$(-i\omega+\nu)\delta f_n+\hat{L}_{n,m}\delta f_m=(-i\omega+\nu)\delta f_n+\hat{L}_{0n,m}\delta f_m + vf_0\left(\frac{\partial\delta\Phi}{\partial r}\frac{\delta_n^1+\delta_n^{-1}}{2} + \frac{\ell\delta\Phi}{r}\frac{\delta_n^1-\delta_n^{-1}}{2}\right)=0, \tag{35}$$

where the second equality gives a definition for the operator $\hat{L}_{n,m}$ and the operator $\hat{L}_{0m,n}$ is defined as

$$\hat{L}_{0n,m}\delta f_m=\frac{v}{2}\left(\frac{\partial\delta f_{n-1}}{\partial r}+\frac{\partial\delta f_{n+1}}{\partial r}\right)+\frac{v}{2r}\left[(\ell+1-n)\delta f_{n-1} -(\ell-1-n)\delta f_{n+1}\right]+i(\ell\omega_r-n\Omega_v)\delta f_n + \frac{F_{r_0}}{2}\left[\frac{\partial\delta f_{n-1}}{\partial v}+\frac{\partial\delta f_{n+1}}{\partial v} - \frac{(n-1)\delta f_{n-1}-(n+1)\delta f_{n+1}}{v}\right]. \tag{36}$$

Recalling the boundary conditions Eq. (32), and applying Eq. (34), the boundary conditions become

$$\begin{aligned}&\delta f_n(0,v)=0, \quad n\neq\ell;\\ &\delta f_n(r,0)=0, \quad n\neq 0;\\ &\delta f_n(r,v)\to 0, \quad r,v\to\infty.\end{aligned} \tag{37}$$

The first and second conditions are unconstrained when $n=\ell$ and $n=0$, respectively. Notice that Eq. (35) does not constitute a closed system for δf, since $\delta\Phi$ also appears. We close the system by introducing the Poisson's equation (in our units), linearizing just as we did above

$$\nabla_\ell^2\delta\Phi=-\delta n, \tag{38}$$

$$\delta n\equiv\int d^2v\,\delta f=2\pi\int dv\,v\,\delta f_{n=0}, \tag{39}$$

where the final identity comes from integrating Eq. (34), where all but the $n=0$ term drops out.

To drive the plasma with $\ell\neq 0$ forcing, a forcing potential on the wall $\delta\Phi_W(r_W,\theta;t)=\delta\Phi_W e^{-i\omega t+i\ell\theta}$ is introduced (expressed here with full θ and t dependence), which serves as a boundary condition for the Poisson's equation, namely, that $\delta\Phi(r_W)=\delta\Phi_W$. (We discuss $\ell=0$ forcing in Sec. VIII D.) We facilitate the solution by splitting the perturbed potential into a sum: $\delta\Phi=\delta\Phi_{\rm H}+\delta\Phi_p$, where $\delta\Phi_{\rm H}$ satisfies the Laplace's (homogeneous) equation $\nabla_\ell^2\delta\Phi_{\rm H}=0$ subject to $\delta\Phi_{\rm H}(r_W)=\delta\Phi_W$, with solution $\delta\Phi_{\rm H}=\delta\Phi_W(r/r_W)^\ell$, and the plasma potential $\delta\Phi_p$ satisfies the (inhomogeneous) Poisson's equation $\nabla_\ell^2\delta\Phi_p=-n$, with Dirichlet boundary conditions. By rewriting our equation in terms of $\delta\Phi_p$, $\delta\Phi_{\rm H}$ appears as a source term, so Eq. (35) becomes

$$[(-i\omega+\nu)\delta_{n,m}+\hat{L}_{{\rm p}n,m}]\delta f_m = -vf_0\left(\frac{\partial\delta\Phi_{\rm H}}{\partial r}\frac{\delta_n^1+\delta_n^{-1}}{2}+\frac{\ell\delta\Phi_{\rm H}}{r}\frac{\delta_n^1-\delta_n^{-1}}{2}\right), \tag{40}$$

where $\hat{L}_{\rm p}$ specifies that the terms proportional to $\delta\Phi$ in $\hat{L}$ of Eq. (35) are to be replaced with $\delta\Phi_p$ (that is, they solve the Poisson's equation with Dirichlet boundary conditions). The resulting linearized Vlasov equation, along with the Poisson's equation and the definition of δn, is

$$\begin{aligned}\left[(-i\omega+\nu)\delta_{n,m}+\hat{L}_{{\rm p}n,m}\right]\delta f_m&=-\frac{\ell\, r^{\ell-1}v f_0\,\delta\Phi_W\,\delta_n^1}{r_{\rm w}^\ell},\\ 2\pi\int dv\,v\,\delta f_{n=0}-\delta n&=0,\\ \nabla_\ell^2\delta\Phi_p+\delta n&=0.\end{aligned} \tag{41}$$

We now regard Eq. (41) as a system of equations for the functions δf_n, δn, $\delta\Phi_p$, written in some basis. The equations have been expressed so that the terms linear in the variables appear on the left-hand side, while sources appear on the right-hand side. For the numerical work considered here, the basis chosen is obtained simply by discretizing the phase space variables r and v. The explicit discretization used will be discussed in Sec. IV A.

The reader may wonder why $\delta\Phi_p$ appearing in Eq. (35) wasn't simply expressed in terms of Green's functions, which are themselves functions of δn and therefore δf. We originally approached the problem this way, but when we began calculating on high-resolution grids we found that the non-local nature of the Green's function (in both space and velocity variables) introduced terms connecting every $n=0$ grid point to every other, making the resulting matrix equation extremely dense. While treating δf, δn, and $\delta\Phi_p$ may appear redundant, the sparsity obtained by introducing a local Poisson's equation rather than non-local Green's function relations far outweighs the marginally increased size of the matrix equation.

We now show that $\hat{L}_0$ is anti-Hermitian with respect to the inner product

$$(a,b)\equiv\sum_{n=-\infty}^{\infty}\langle a_n|b_n\rangle, \tag{42}$$

where

$$\langle a_n|b_n\rangle\equiv\int_0^\infty r\,dr\int_0^\infty v\,dv\,a_n^*(r,v)\,b_n(r,v). \tag{43}$$

The anti-Hermitian property ensures that, in the absence of self-consistent effects, normal mode frequencies are purely real. This is to be expected, since $\hat{L}_0$ describes a plasma of test charges moving in a background field, which should not have modes that grow or decay indefinitely. On the other hand, if a numerical method was employed that does not satisfy this anti-Hermitian property, spurious growth or decay of modes could occur. This possibility will be addressed when we discuss the discretization of the equations.

To prove the anti-Hermitian property, we rewrite $\hat{L}_0$ by rewriting r and v derivatives using

$$\begin{aligned}\frac{\partial f_n}{\partial r}(r,v)&=\frac{1}{\sqrt{r}}\frac{\partial}{\partial r}\left[\sqrt{r}f_n(r,v)\right]-\frac{1}{2r}f_n(r,v),\\ \frac{\partial f_n}{\partial v}(r,v)&=\frac{1}{\sqrt{v}}\frac{\partial}{\partial v}\left[\sqrt{v}f_n(r,v)\right]-\frac{1}{2v}f_n(r,v),\end{aligned}$$

which gives

$$\hat{L}_{0n,m}f_m = \frac{v}{2}\left(\frac{1}{\sqrt{r}}\frac{\partial}{\partial r}\left[\sqrt{r}(\delta f_{n-1}+\delta f_{n+1})\right] + \frac{(\ell+1/2-n)\delta f_{n-1} - (\ell-1/2-n)\delta f_{n+1}}{r}\right) + i(\ell\omega_r - n\Omega_v)\delta f_n + \frac{F_{r_0}}{2}\left(\frac{1}{\sqrt{v}}\frac{\partial}{\partial v}\left[\sqrt{r}(\delta f_{n-1}+\delta f_{n+1})\right] - \frac{(n-1/2)\delta f_{n-1} - (n+1/2)\delta f_{n+1}}{v}\right). \quad (44)$$

We now form the inner product $(g,\hat{L}_0 f)$. We then apply the following identities, proved through integration by parts:

$$\left\langle g_m \middle| \frac{1}{\sqrt{r}}\frac{\partial}{\partial r}\left[\sqrt{r}f_n\right]\right\rangle = -\left\langle \frac{1}{\sqrt{r}}\frac{\partial}{\partial r}\left[\sqrt{r}\,g_m\right]\middle| f_n\right\rangle, \quad (45)$$

$$\left\langle g_m \middle| \frac{1}{\sqrt{v}}\frac{\partial}{\partial v}\left[\sqrt{v}f_n\right]\right\rangle = -\left\langle \frac{1}{\sqrt{v}}\frac{\partial}{\partial v}\left[\sqrt{v}\,g_m\right]\middle| f_n\right\rangle, \quad (46)$$

$$\left\langle g_n \middle| \left(\ell-n+\frac{1}{2}\right)f_{n-1} - \left(\ell-n-\frac{1}{2}\right)f_{n+1}\right\rangle = -\left\langle \left(\ell-n+\frac{1}{2}\right)g_{n-1} - \left(\ell-n-\frac{1}{2}\right)g_{n+1}\middle| f_n\right\rangle, \quad (47)$$

which demonstrate that all terms appearing in $\hat{L}_0$ are anti-Hermitian: $(g,\hat{L}_0 f) = -(\hat{L}_0 g, f)$.

A. Numerical grid

The next step is to put Eq. (35) on a grid to be solved computationally. First, we only keep a finite number of gyroharmonics in the solution, $|n| < M_\psi$ for a given integer M_ψ chosen to be sufficiently large to yield convergent results (more on this later). For $n-$values beyond this range, we set $\delta f_n = 0$. We choose a uniform radial grid with $r_i = i\Delta r$, $i = 0,1,2,\ldots,M_r$, and a uniform grid in speed v with $v_j = j\Delta v$, $j = 0,1,2,\ldots,M_v$, writing $\delta f_n(r_i,v_j) \equiv \delta f^n_{i,j}$. The maximum radius $R_{max} = M_r\Delta r$ is chosen to be just outside the plasma, and the maximum speed $V_{max} = M_v\Delta v$ is chosen to be roughly 4 thermal speeds, i.e., in scaled units $V_{max} \approx 4$. We discretize the operator using second-order-accurate centered-differences for the derivatives in r and v.

However, this introduces small, unphysical errors because the discretized operator $\hat{L}_{0n,m}$ is no longer anti-Hermitian. These errors can have the effect of destabilizing the equations, creating instabilities that result in spurious grid-scale oscillations in the wave potential and unphysical peaks in the admittance. This can be ameliorated by carefully choosing a discretization scheme that preserves the anti-Hermitian property as much as possible. One such method rewrites the radial derivatives in Eq. (36) as $\partial f/\partial r = (1/r)\partial(rf)/\partial r - f/r$, and similarly for the v-derivatives, then center-differences these derivatives while averaging some terms over neighboring grid-points in r and v, as in the Lax method.[13] With this modification, the differenced Eq. (35) becomes

$$\frac{v_j}{2r_i}\left(\frac{r_{i+1}(\delta f^{n+1}_{i+1,j}+\delta f^{n-1}_{i+1,j}) - r_{i-1}(\delta f^{n+1}_{i-1,j}+\delta f^{n-1}_{i-1,j})}{2\Delta r} - \frac{n}{2}(\delta f^{n-1}_{i+1,j} - \delta f^{n+1}_{i+1,j} + \delta f^{n-1}_{i-1,j} - \delta f^{n+1}_{i-1,j}) + \ell(\delta f^{n-1}_{i,j} - \delta f^{n+1}_{i,j})\right)$$
$$+\frac{F_{r0i}}{2v_j}\left(\frac{v_{j+1}(\delta f^{n+1}_{i,j+1}+\delta f^{n-1}_{i,j+1}) - v_{j-1}(\delta f^{n+1}_{i,j-1}+\delta f^{n-1}_{i,j-1})}{2\Delta v} - \frac{n}{2}(\delta f^{n-1}_{i,j+1} - \delta f^{n+1}_{i,j+1} + \delta f^{n-1}_{i,j-1} - \delta f^{n+1}_{i,j-1})\right)$$
$$+\frac{v_j f_{0i,j}}{2}\left(\frac{\delta\Phi_{i+1}-\delta\Phi_{i-1}}{2\Delta r}(\delta_{n,1}+\delta_{n,-1}) + \frac{\ell\delta\Phi_i}{r_i}(\delta_{n,1}-\delta_{n,-1})\right) + i(\ell\omega_r + n\Omega_v - \omega - i\nu)\delta f^n_{ij} = -\frac{\ell r_i^{\ell-1}v_j f_{0i,j}\delta\Phi_W\delta^1_n}{r_w^\ell}. \quad (48)$$

In both the first and second lines, the two terms proportional to n are written as the average over their neighboring grid-points in r and v, respectively, which is correct as the grid size approaches zero. Using the discretized version of Eq. (42), where the integrals are replaced with a Simpson's rule Riemann sum, this discretized Vlasov equation is also anti-Hermitian in the absence of the self consistent $\delta\Phi_p$ term, with respect to the anti-Hermiticity of the continuous equation. This equation forms a closed linear inhomogeneous system of equations when combined with discretized forms of the density relation and Poisson's equation shown as follows:

$$2\pi\sum_{j=0}^{M_v-1}\frac{1}{2}(v_j\delta f^0_{i,j} + v_{j+1}\delta f^0_{i,j+1}) - \delta n_i = 0, \quad (49)$$

$$\frac{\delta\Phi_{i+1}-2\delta\Phi_i+\delta\Phi_{i-1}}{\Delta r^2} + \frac{\delta\Phi_{i+1}-\delta\Phi_{i-1}}{2r_i\Delta r} - \frac{\ell^2}{r_i^2}\delta\Phi_i + \delta n_i = 0, \quad (50)$$

along with the boundary conditions from Eq. (37)

$$\delta f^n_{0,j} = 0, \quad n \neq \ell; \quad (51)$$

$$\delta f^\ell_{0,j} = 2f^\ell_{1,j} - f^\ell_{2,j}; \quad (52)$$

$$\delta f^n_{i,0} = 0, \quad n \neq 0; \quad (53)$$

$$\delta f^0_{i,0} = 2f^\ell_{i,1} - f^\ell_{i,2}; \tag{54}$$

$$\delta f^n_{M_r,j} = \delta f^n_{i,M_v} = 0, \tag{55}$$

where Eqs. (52) and (54) determine the free gridpoints through linear interpolation for the special cases at the radial origin where $n = \ell$, or at the velocity origin where $n = 0$. Equations (48)–(50) are used for internal points $i = 1, \ldots, M_r - 1$, $j = 1, \ldots, M_v - 1$. The boundary condition on the discretized perturbed plasma potential $\delta\Phi_i$ is obtained by matching at $i = M_r$ to a solution to the Laplace equation that vanishes at the wall: $\delta\Phi_{M_r} = \delta\Phi_p(R_{max}) = C(R^\ell_{max} - (r^2_W/R_{max})^\ell)$, where the constant C is obtained by matching the derivative, $\delta\Phi'_p(R_{max}) = C\ell(R^\ell_{max} + (r^2_W/R_{max})^\ell)/R_{max}$. (The left-hand side of this equation is discretized in the usual way).

B. Convergence

It is of critical importance to ensure that numerical results are properly converged; in this problem, numerical accuracy is improved by increasing the number of grid points in r and v (namely, M_r and M_v), as well as by increasing the number of gyroharmonics (namely, M_ψ) kept in the calculation. Some exploration is required to discover optimal values for each of these three numbers, as the results obviously need to be converged in all three variables simultaneously in order to have reliable results. When checking for convergence, M_r and M_v were independently incremented by 30 at a time, and M_ψ was incremented by two at a time. In this paper, we report on three ℓ values, $\ell = 0, 2$, and 4. Convergence issues varied in each case.

We found that, in general, M_r and M_v must be increased as the damping ν decreases. This is because we are approximating the frequency response of our mathematical plasma with a sufficiently large, discrete matrix equation whose eigenfrequencies (magnetized van Kampen[14] modes) must do a decent job of covering the frequency range of interest. As ν decreases, the resonance width of these discrete (numerical) modes will eventually become smaller than their spacing, at which point the results become unphysical. In order to probe finer frequency resolution, the number of eigenvalues must be increased, which is conveniently done by increasing M_r and M_v. This type of numerical issue typically manifests itself as an admittance function with extremely sharp peaks that do not persist as resolution is increased or move around unpredictably as the grid is adjusted slightly. The problem is resolved either by increasing ν (if less frequency resolution is tolerable), or else by increasing M_r and M_v.

For the finite damping rates used in the paper, convergence in the admittance results was obtained with a relatively small M_ψ value compared to the number of r and v grid points required: $M_\psi \sim 10$ was usually sufficient. For $\ell = 4$, the values of M_r and M_v required for convergence were $M_r \sim M_v \sim 100$. This resolution was sufficient to resolve the first four to eight admittance peaks, counting from the right (see Fig. 4); lower frequency peaks beyond this range correspond to potentials that oscillate more rapidly in r, requiring higher resolution. Somewhat higher resolution was also typically required at larger magnetic fields.

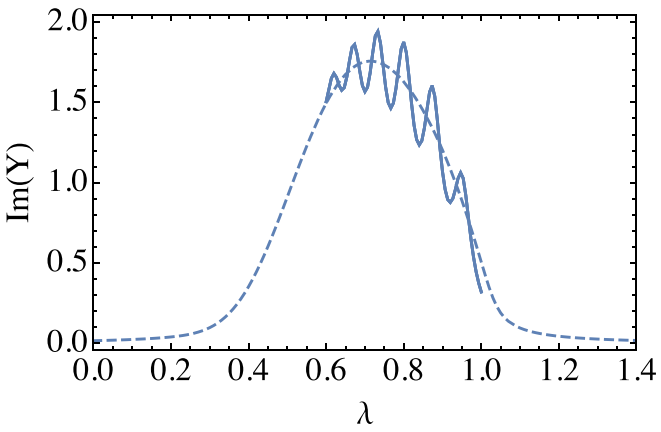

FIG. 4. Imaginary part of the admittance versus scaled frequency λ for $\ell = 2$ and $\Omega = 5$ in a plasma with $R_p = 4.76$, $r_W = 10$, and collision frequency $\nu = 0.00283$. (i.e., the same parameters as in Figs. 2 and 3, but with finite ν rather than $\nu = 0$). Solid line: Vlasov solution. Dashed line: cold fluid theory.

For $\ell = 2$, larger values of M_r and M_v had to be used to resolve just the first few admittance peaks, up to $M_r = M_v = 240$ and $M_\psi = 10$, the maximum values we could run on the available computers (limited by memory requirements in the numerical solution of the sparse matrix equation).

We should also mention that there were convergence issues in the distribution function near $r = 0$ for $\ell = 2$; namely, rapid unphysical variation in δf_n versus r and v, for r within a thermal cyclotron radius or so of $r = 0$. The origin of this rapid variation is unknown, but is clearly an artifact of the discretization of the linear operator. For $\ell = 4$, the wave potential is small enough near the origin so that this effect was suppressed, since δf is quite small near the origin. However, in all ℓ values studied this unphysical variation did not seem to affect the density or potential, which was well-converged and varied smoothly with radius near $r = 0$.

In test cases we studied, where the solution for $\delta f(r, \theta, v, \psi)$ near $r = 0$ is known analytically for a given perturbed potential (as a power series expansion in r), the discretized Vlasov equation was able to reproduce the analytical solution for the perturbed density and plasma potential response, even though the numerical distribution function was noisy near the origin. As a second check, for $l = 2$ we added 4th derivative "superdiffusion" terms in r and v to the discretized Vlasov equation in order to suppress this grid-scale noise in the distribution function near $r = 0$, and found that for a scaled superdiffusion coefficient of 10^{-6} the solution reproduced the admittance curves without superdiffusion, with far less noise in δf_n near $r = 0$. These checks gave us some confidence that the admittance, density, and potential results were sensible even when the underlying distribution function was noisy near the origin.

For $\ell = 0$, and for the "hot" $r_p = 4.76$ plasma discussed in relation to Figs. 2 and 3, it was fairly easy to obtain converged admittance results for moderate values of the grid parameters and moderately strong damping rates, similar to those used in the $\ell = 4$ data. No noise issues near the radial origin were observed. For a colder plasma we studied, with $r_p = 43$, more radial grid points had to be used in order to resolve the plasma edge, as one would expect.

Finally, we encountered a puzzling anomaly that caused numerical instability for $v > v_{\text{thresh}}$, where v_{thresh} depended on the radial grid spacing Δr, M_ψ. When this instability was present, the perturbed distribution function in phase space would look normal for small velocities, but for $v > v_{\text{thresh}}$ would appear random. It was discovered that this instability could be avoided by increasing the quantity $\Delta r M_\psi / V_{\max}$, where $V_{\max}$ is the highest velocity on the grid, thereby forcing v_{thresh} higher than the highest velocity kept on the grid. Therefore, we only increase M_r (i.e., decrease Δr) as much as is needed to resolve the radial variation in the mode, but no more, unless we are willing to increase M_ψ.

C. Results

In Fig. 4, we display a characteristic solution taken from the converged results of the numerical Vlasov code [i.e., the solutions of (48)–(50)] for the imaginary part of the admittance function versus scaled frequency λ [see Eq. (27)]. The plasma is assumed to have the same parameters as in Figs. 2 and 3, except that in those figures $\nu = 0$, whereas here we take $\nu = 0.00283$. (As previously mentioned, a finite value of ν is necessary to obtain converged results in the Vlasov solution.) One can see that the admittance has separated into a series of peaks whose magnitudes follow the corresponding cold fluid theory, and whose spacing varies, becoming more closely spaced as frequency λ decreases. Each peak corresponds to a Bernstein mode.

Incidentally, the cold fluid theory admittance plotted in Fig. 3 differs slightly from the theory presented in Sec. III in that we took $\nu \neq 0$ for Fig. 4, just as in the Vlasov theory. For finite ν, the radial dependence of cold fluid theory potential differs only slightly from that shown in Fig. 2; the sharp singularity at the upper hybrid cutoff radius r_{UH0} becomes slightly rounded.

In Fig. 5, the radial dependence of the Vlasov-theory perturbed potential is plotted for λ values at three of the peaks. Inside the cutoff, the potential oscillates with radius. These oscillations are the Bernstein normal modes. For radii larger than the upper hybrid cutoff r_{UH0} (shown by the arrow in each figure), the potential decays in a fashion similar to the cold fluid theory shown in Fig. 2; here, the Bernstein modes are evanescent. As scaled frequency λ decreases, the wavelength of the modes decreases as well.

V. NEW WKB TREATMENT

In order to understand the results of the Vlasov code, we turn to WKB theory descriptions of the electrostatic Bernstein modes. We first review the modes in a uniform plasma and then discuss a new WKB theory for the modes in a plasma column with nonuniform density versus radius. This WKB theory further develops a previous theory,[1] providing an improved description of the mode frequencies.

A. Dispersion relation

In a uniform plasma, that rotates uniformly with frequency ω_f, the dispersion relation for electrostatic waves traveling perpendicular to the magnetic field is given by[15]

$$0 = 1 - \omega_p^2 \sum_{n=-\infty}^{\infty} \frac{n^2 e^{-\Lambda} I_n(\Lambda)}{\Lambda(\hat{\omega}^2 - n^2 \Omega_v^2)}, \quad \text{with } \Lambda \equiv k^2 r_c^2. \tag{56}$$

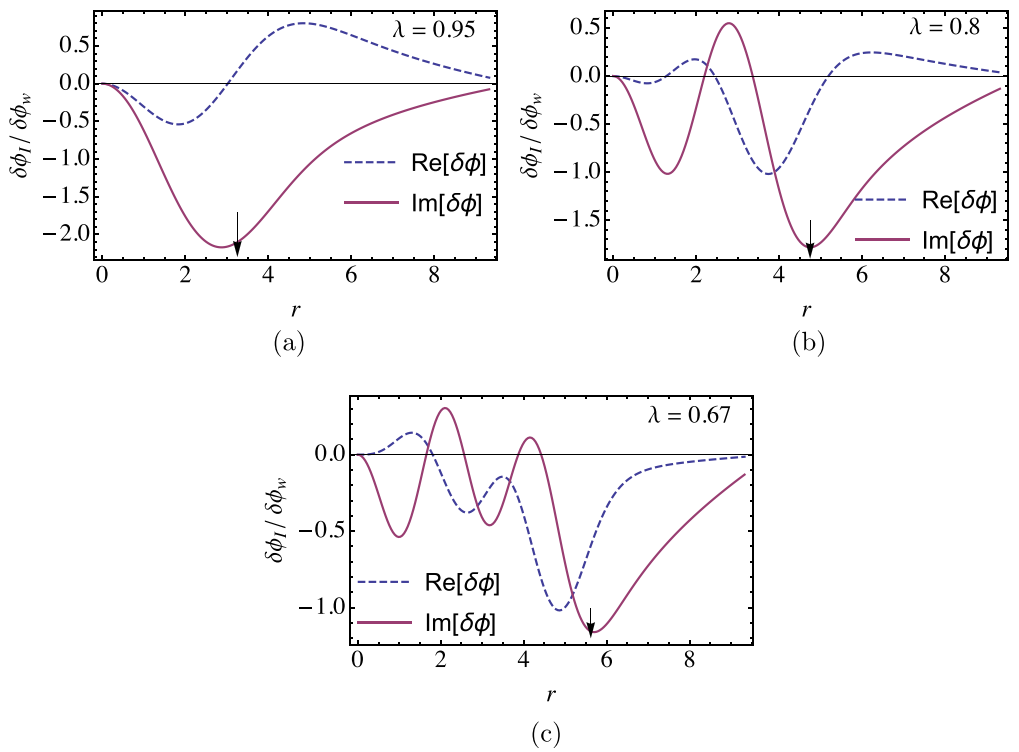

FIG. 5. Radial dependence of the Vlasov solution for the real and imaginary part of the plasma wave potential $\delta\Phi_p$, for λ values at three peaks in the previous admittance figure: the first, third, and fifth peaks counting from right to left. This potential does not include the driving potential $\delta\Phi_H$ and therefore vanishes at the wall radius $r_W = 10$. (a) First mode, (b) third mode, and (c) fifth mode.

Here, k is the wavenumber, $\hat{\omega}$ is the Doppler-shifted driving frequency (including Krook collisions) seen in the frame rotating with the plasma, defined by $\hat{\omega} = \omega - \ell\omega_f + i\nu$, r_c is the thermal cyclotron radius given by $r_c = 1/\Omega_v$ in scaled units, and $I_n(x)$ is a modified Bessel function. To study these modes near the cyclotron frequency, we ignore all but the dominant terms in which the denominator is small with $n = \pm 1$. With this simplification, the dispersion function becomes

$$\mathcal{D}(\omega, k) = 1 - 2\omega_p^2 \frac{e^{-\Lambda} I_1(\Lambda)}{\Lambda(\hat{\omega}^2 - \Omega_v^2)}. \tag{57}$$

This expression can be related to the fluid theory dispersion relation involving the function $X(\omega)$ as follows (noting that X simplifies for a uniform system):

$$\mathcal{D}(\omega, k) = 1 - 2X(\omega) \frac{e^{-\Lambda} I_1(\Lambda)}{\Lambda}. \tag{58}$$

Note that the function $2e^{-\Lambda} I_1(\Lambda)/\Lambda$ is monotonically decreasing in Λ with a maximum of unity at $\Lambda = 0$. Thus, a solution to $\mathcal{D} = 0$ requires that $X(\omega) > 1$, or equivalently $\epsilon_{11} < 0$. Thus, propagating Bernstein waves can exist in the plasma only for frequencies for which $\epsilon_{11} < 0$. However, if $\epsilon_{11} > 0$ there are still solutions to $\mathcal{D} = 0$, but these solutions require imaginary values of k (i.e., negative Λ). These are evanescent (non-propagating) solutions.

The frequency versus (real) wavenumber following from $\mathcal{D} = 0$ is plotted in Fig. 6. The dispersion curve demonstrates that zero wavenumber corresponds to waves at the upper-hybrid frequency $\hat{\omega} = \sqrt{\Omega_v^2 + \omega_p^2}$, whereas for a larger wavenumber, cyclotron orbits tend to "average out" the effect of the perturbed electric field, lowering the mode frequency toward the bare cyclotron frequency in the rotating frame, $\hat{\omega} = \Omega_v$.

In geometrical optics, the $k \to 0$ limit corresponds to a classical turning point for a ray trajectory. Figure 6 shows that this limit occurs at the upper hybrid frequency, where $\epsilon_{11} = 0$. Therefore, in an inhomogeneous plasma the locations where

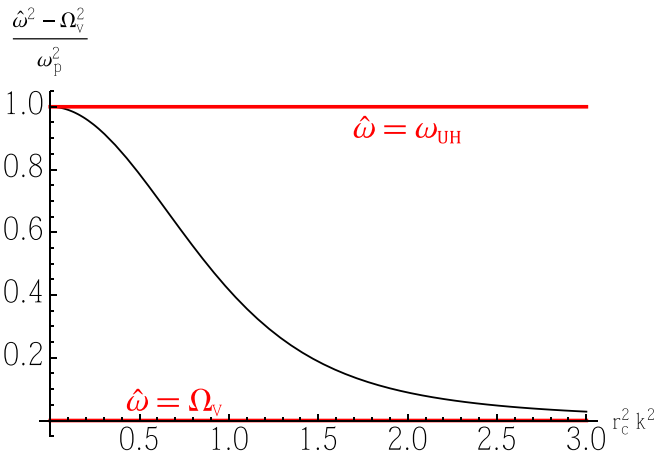

FIG. 6. Dispersion relation plotted as $\frac{\hat{\omega}^2 - \Omega_v^2}{\omega_p^2}$ versus $r_c^2 k^2$. At low kr_c, $\hat{\omega}$ limits to the upper-hybrid frequency, while for high kr_c, it limits to the vortex frequency.

the mode frequency matches the upper hybrid frequency are classical turning points. These locations are marked by the arrows in Fig. 5, and explain qualitatively why the Bernstein waves change behavior from propagating modes with $\epsilon_{11} < 0$ to evanescent decay with $\epsilon_{11} > 0$. The reflection of the wave at the upper hybrid radius is what sets up a radial normal mode of oscillation within the plasma column. In Secs. V B–V F, a more detailed WKB analysis verifies this picture and also shows how the Bernstein waves mode-couple to surface cyclotron waves at the upper hybrid radius.

Before we do so, however, it is useful to briefly consider the general form of the Bernstein differential equation in a uniform, isotropic rotating plasma by appealing to symmetry arguments. (For example, the dispersion relation in Eq. (56) for a uniform plasma could be derived from a differential equation of this form). This will allow us to obtain expressions for the spatial dependence of the Bernstein wave potential in such a system.

In the plasma center where the system is spatially uniform and rotationally invariant, the differential operator $\mathcal{D}$ must respect these symmetries. Consider expanding $\mathcal{D}$ in a series of increasing differential order, with tensor $T^{(n)}$ as the expansion coefficients

$$\mathcal{D} = \sum_n \underbrace{T^{(n)}_{\cdots}\, \partial_\cdot \partial_\cdot \cdots \partial_\cdot}_{n \text{ index contractions}}. \tag{59}$$

If $\mathcal{D}$ is to be isotropic, then each of the $T^{(n)}$ must be invariant under rotations. Necessary and sufficient conditions for tensor isotropy have been determined to be linear combinations of products of Kronecker Delta tensors and possibly a single Levi Cevita tensor ε.[16,17] Therefore, $\mathcal{D}$ can be expressed schematically as

$$\mathcal{D} = \sum_n \underbrace{\{\delta_{\cdot\cdot}\delta_{\cdot\cdot} \cdots \delta_{\cdot\cdot}\varepsilon_{\cdot\cdot}\}\partial_\cdot \partial_\cdot \cdots \partial_\cdot}_{n \text{ index contractions}}, \tag{60}$$

where $\{\}$ denotes a linear combination of expressions of the form of its contents. Notice that any case where a given δ involves a self-contraction can be ignored, since this only introduces a factor of the dimension, here 2. Similarly, any self-contraction within ε vanishes due to antisymmetry. Furthermore, any contractions pairing a δ with either another δ or with ε can also be ignored, since either such contraction amounts to renaming a dummy index. Consequently, all indices must contract with a derivative. This immediately implies that every term in $\mathcal{D}$ has an even number of derivatives, that is, twice the number of symbols (δ or ε) appearing in that term (only terms with even n in the sum contribute). Using commutativity of the Kronecker Delta, Levi Cevita, and partial derivatives, this allows us to write each term in the standard form, this time giving the indices unique labels

$$\mathcal{D} = \sum_{\text{even } n} \delta_{i_1 i_2}\delta_{i_3 i_4} \cdots \left(A^{(n)}\delta_{i_{n-1}\, i_n} + B^{(n)}\varepsilon_{i_{n-1}\, i_n}\right) \times \partial_{i_1}\partial_{i_2}\partial_{i_3}\partial_{i_4} \cdots \partial_{i_{n-1}}\partial_{i_n}, \tag{61}$$

where $A^{(n)}$ and $B^{(n)}$ are arbitrary coefficients. Finally, we can write this expression in vector form

$$\mathcal{D} = \sum_{i=0}^{\infty} (\nabla^2)^i \nabla \cdot E^{(i)} \nabla, \tag{62}$$

where

$$E^{(i)} = \begin{pmatrix} A^{(i)} & B^{(i)} \\ -B^{(i)} & A^{(i)} \end{pmatrix}.$$

To match this general form of $\mathcal{D}$ to the fluid theory of Sec. III, we impose the additional constraint that $E^{(0)} = \epsilon$ (recall ϵ is the fluid theory dielectric) so that the theories match to the lowest differential order. Since Bessel Functions of the first and second kind are always eigenfunctions of ∇^2 and $\nabla \cdot E^{(i)} \nabla$, we can see that $CJ_\ell(kr) + DY_\ell(kr)$ satisfies this equation and continuity at $r = 0$ enforces $D = 0$. Furthermore, since $J_\ell(kr)$ is locally asymptotic to a plane wave with wavenumber k far from the origin, k must satisfy $\mathcal{D}(\omega, k) = 0$. While this solution is only valid for a uniform plasma, it also provides an approximate solution to a physical plasma for $r \ll r_p$, where $n(r)$ is very nearly constant. This expression allows us to connect the WKB expression (valid away from the origin) to this Bessel Function solution near the center of the plasma.

B. WKB regions

To calculate Bernstein modes in a non-uniform cylindrical plasma, we use a WKB approach. We assume a single-species plasma for which there is a range of frequencies near the cyclotron frequency with a single solution to Eq. (18), i.e., a single upper hybrid radius. In other words, ϵ_{11} increases monotonically with radius from a negative value inside the plasma, through zero at the upper hybrid radius, and increasing toward unity outside the plasma. In this case, there will be a propagating Bernstein wave for radii less than r_{UH0}, becoming evanescent for $r > r_{\mathrm{UH0}}$, as in the numerical results shown in Fig. 5.

In the WKB analysis of these waves, we find that the perturbed potential can be expressed as a combination of a fluid theory solution and a radially oscillating Bernstein wave

$$\delta\Phi = \overline{\delta\Phi} + \widetilde{\delta\Phi}, \tag{63}$$

where $\widetilde{\delta\Phi}$ is the radially oscillating Bernstein wave emerging from finite temperature effects and $\overline{\delta\Phi}$ is the non-oscillatory fluid theory. For radii far from the upper hybrid cutoff, the fluid theory solution is slowly varying in r and thermal corrections are negligible. We can therefore use cold-fluid theory to describe this solution, numerically integrating Eq. (11) to obtain $\overline{\delta\Phi}$ away from the upper hybrid cutoff. For the Bernstein solution, on the other hand, we employ the WKB eikonal approach, matching inner and outer forms for the eikonals across the upper hybrid radius.

A schematic of the full solution is shown in Fig. 7. We break the solution into 3 overlapping regions, treated with different methods, and match the solution across the regions. In the central region close to $r = 0$, the plasma is nearly uniform and we use the Bessel function solution for the

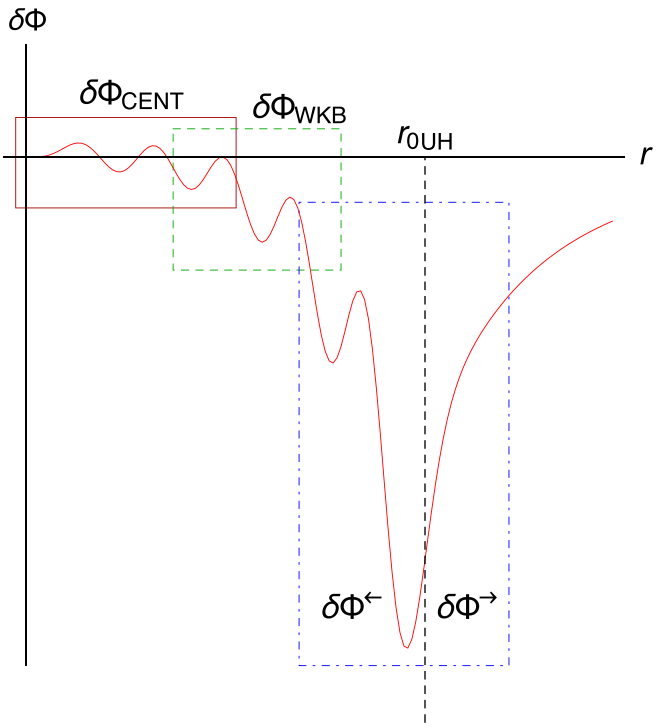

FIG. 7. A plot of a typical $\delta\Phi$ showing the three main regions of the plasma: $\delta\Phi_{\mathrm{CENT}}$, $\delta\Phi_{\mathrm{WKB}}$, $\delta\Phi^{\leftarrow}$ and $\delta\Phi^{\rightarrow}$ referred to in the WKB theory. The region far outside the plasma is not given a name because it trivially satisfies Laplace's equation and has no Bernstein waves.

Bernstein wave, derived in Sec. V A. For intermediate radii between $r \gtrapprox 0$ and the upper hybrid cutoff at $r \lessapprox r_{\mathrm{UH}}$, WKB theory is used. In this region, the Bernstein solution is oscillatory. As we pass through the upper hybrid cutoff, the Bernstein solution transitions from oscillatory to evanescent. Within this transition region near the cutoff, we solve an approximate form of the Bernstein differential operator to match solutions across the cutoff. Here, we find that the Bernstein solution mode-couples to the fluid solution, mixing the two in this transition region. A jump condition on the fluid solution across the transition region is obtained, describing the effect of this mode coupling on the fluid solution. A similar jump condition was obtained in Ref. 1, the difference here being that the fluid solution is treated exactly (via numerical solution) rather than using an approximate analytical form valid only for large magnetic field as in Ref. 1.

C. Central solution

We begin with the solution valid near the center of the plasma, where the density $n(r)$ is nearly constant for a thermal equilibrium plasma. As we derived previously, the oscillatory Bernstein solution for a uniform plasma takes the form of a Bessel function

$$\widetilde{\delta\Phi}(r) = A_{\mathrm{cent}} J_\ell(k_0 r), \tag{64}$$

where, for given ω, k_0 is the solution for k of the Bernstein dispersion relation, Eq. (58), at the center of the plasma. In order for this solution to match with the Eikonal solution

described in Sec. V D, we use the large argument expansion for $J_\ell(z)$, giving

$$\widetilde{\delta\Phi}_{\text{cent}} \sim A_{\text{cent}}\sqrt{\frac{2}{\pi k_0 r}}\cos\left(k_0 r - \frac{\ell\pi}{2} - \frac{\pi}{4}\right). \tag{65}$$

D. Eikonal form

Since a thermal equilibrium plasma does not have a uniform density profile $n(r)$, the Bessel function solution introduced in Sec. V C is not satisfactory to describe the entire interior of the plasma. While the asymptotic central result in Eq. (65) is a constant wavenumber solution, we now require k to change as a function of r as the dispersion relation changes due to the nonuniform plasma density. This motivates a WKB approach to be accurate in the limit where $k \gg |k'(r)/k|$. To the lowest order in WKB theory, the form of $k(r)$ is found for given ω by solving Eq. (58), with X and Ω_v the functions of r appropriate for given $n(r)$. This approximation is only valid away from the cutoff where $k \to 0$. This solution is used in the Eikonal in the region that is both far to the left of the cutoff, and also far from $r = 0$

$$\widetilde{\delta\Phi}_{\text{wkb}} = A(r)\cos\left(\int_{r_{\text{UH}}}^{r} k(\bar{r})\, d\bar{r} + \chi\right), \tag{66}$$

where $A(r)$ is a slowly varying amplitude, the local wavenumber $k(r)$ is found from the Bernstein dispersion relation Eq. (58) (for given frequency ω), and χ is a phase factor to be determined momentarily. The radial form of the amplitude factor is not needed in what follows, but was discussed in Ref. 1.

Matching the central Eq. (65) and WKB Eq. (66) solutions gives the connection formula that determines the phase factor χ

$$\chi = \int_0^{r_{\text{UH}}} k\, dr - \frac{\ell\pi}{2} - \frac{\pi}{4}. \tag{67}$$

E. Upper-hybrid cutoff

Near the cutoff, where $\omega_{\text{UH}} - \hat{\omega} \to 0$, the wavenumber of the WKB solutions also approaches zero (see Fig. 6), so we can consider adding finite cyclotron radius effects perturbatively into Eq. (6)

$$0 = \nabla\cdot\epsilon\nabla\delta\Phi - r_c^2\nabla^2\big((1-\epsilon_{11})\nabla^2\delta\Phi\big). \tag{68}$$

This approximate expression can be checked by replacing ∇ with $i\mathbf{k}$ and comparing the result with Eq. (58), expanding this dispersion relation to the fourth order in k. However, it should be noted that this check only verifies the factor $1-\epsilon_{11}$, but does not justify its algebraic location between the two Laplacians. Dubin[1] shows, by using integration over unperturbed orbits in the large magnetic field limit, why this factor appears in the location it does here. Equation (68) generalizes the warm fluid theory mode equation of Ref. 1 by not taking the large magnetic field limit. This generalization is important in helping to explain a discrepancy between the numerical Vlasov solution and the large magnetic field WKB analysis of Ref. 1.

We should emphasize that while Eq. (68) is consistent with the uniform plasma dispersion relation in the small wavenumber limit, many other forms of the equations could also be consistent. In fact, Dubin showed that many other terms appear at $\mathcal{O}(r_c^2)$ in the warm fluid theory equation in the large magnetic field limit; but he also showed that the other terms were subdominant in the WKB approximation. We have no way of knowing what the form of such terms are when the large magnetic field limit is not taken, so we cannot prove that such terms are also subdominant to those kept in Eq. (68). This equation should therefore be regarded skeptically, as an educated guess.

We use Eq. (68) only near the upper hybrid radius and so we will now approximate its form in this region. Writing out Eq. (68) in cylindrical coordinates, and multiplying by r_c^2 to make each term dimensionless, we examine the resulting terms and drop those terms containing one or more factors of $\frac{r_c}{r}$, since the upper-hybrid radius is assumed to be many cyclotron radii from the origin. The result leaves the following:

$$-r_c^4(1-\epsilon_{11})\delta\Phi^{(4)} + 2r_c^4\epsilon'_{11}\delta\Phi^{(3)} + r_c^2(\epsilon_{11} + r_c^2\epsilon''_{11})\delta\Phi'' + r_c^2\epsilon'_{11}\delta\Phi' = 0.$$

By repeated use of the product rule, this can be partially integrated to obtain

$$r_c^2\frac{\partial}{\partial x}\left[(1-\epsilon_{11})\delta\Phi''\right] - \epsilon_{11}\delta\Phi' = C, \tag{69}$$

with C a constant of integration (prime represents derivative with respect to x). To connect with the Eikonal Eq. (66), which assumes $\epsilon'_{11}/k \ll 1$, we take the dominant balance of terms, neglecting the term proportional to ϵ'_{11} in the first term of Eq. (69). Furthermore, we use a linear expansion $\epsilon_{11} \sim (r - r_{\text{UH}})/\mathcal{L}$ near the upper-hybrid cutoff radius, defining the plasma scale length

$$\mathcal{L} \equiv 1\Big/\frac{\partial\epsilon_{11}}{\partial r}, \tag{70}$$

and write

$$r_c^2(1-\epsilon_{11})\delta\Phi''' - \frac{r - r_{\text{UH}}}{\mathcal{L}}\delta\Phi' = C. \tag{71}$$

For r near r_{UH}, the appearance of $1-\epsilon_{11}$ in the first term can be replaced with 1, since ϵ_{11} is small compared to 1 and is assumed to change gradually anyways. After making this change, the expression can be manipulated into an inhomogeneous Airy equation by the substitution $r = r_{\text{UH}} + (\mathcal{L}\, r_c^2)^{1/3}\, s$

$$\delta\Phi''' - s\,\delta\Phi' = C'. \tag{72}$$

The solution to the corresponding homogeneous equation for $\delta\Phi'$ is solved by Airy Functions. We can solve the inhomogeneous problem by using variation of parameters to obtain

$$\delta\Phi'(s) = D_1\mathrm{Ai}(s) + D_2\mathrm{Bi}(s) + D_3\mathrm{Ci}(s), \tag{73}$$

where

$$\mathrm{Ci}(s) \equiv \pi\mathrm{Ai}(s)\int_{-\infty}^{s}\mathrm{Bi}(\bar{s})\,d\bar{s} + \pi\mathrm{Bi}(s)\int_{s}^{\infty}\mathrm{Ai}(\bar{s})\,d\bar{s}. \tag{74}$$

The coefficients D_i in Eq. (73) are determined by matching asymptotic forms for the Airy functions to the corresponding asymptotic forms for the potential to the left and right of the cutoff. The asymptotic expansions of the Airy Functions are as follows:

$$\mathrm{Ai}(s) \sim \begin{cases} \dfrac{\sin\left(\frac{2}{3}(-s)^{3/2} + \frac{\pi}{4}\right)}{\sqrt{\pi}(-s)^{1/4}}, & s \to -\infty \\ \dfrac{\exp\left(-\frac{2}{3}(s)^{3/2}\right)}{2\sqrt{\pi}(s)^{1/4}}, & s \to \infty \end{cases}$$

$$\mathrm{Bi}(s) \sim \begin{cases} \dfrac{\cos\left(\frac{2}{3}(-s)^{3/2} + \frac{\pi}{4}\right)}{\sqrt{\pi}(-s)^{1/4}}, & s \to -\infty \\ \dfrac{\exp\left(\frac{2}{3}(s)^{3/2}\right)}{\sqrt{\pi}(s)^{1/4}}, & s \to \infty \end{cases} \tag{75}$$

$$\mathrm{Ci}(s) \sim \begin{cases} \dfrac{1}{s} + \dfrac{\sqrt{\pi}\cos\left(\frac{2}{3}(-s)^{3/2} + \frac{\pi}{4}\right)}{(-s)^{1/4}}, & s \to -\infty \\ \dfrac{1}{s}, & s \to \infty. \end{cases}$$

From these approximations, we can obtain the solution for $\delta\Phi$ by integrating the left-side asymptotic expansion of Eq. (73) once. While the integral is not an elementary function, it can nonetheless be carried out in the asymptotic limit. We can also immediately drop the term containing $\mathrm{Bi}(s)$, since the exponential growth outside the plasma is unphysical. Then, the asymptotic result in the interior of the plasma is

$$\delta\Phi^{\leftarrow}(s) = D_1\left(\frac{-\sin\left(\frac{2}{3}(-s)^{3/2} - \frac{\pi}{4}\right)}{\sqrt{\pi}(-s)^{3/4}}\right) + D_3\left(\frac{-\sqrt{\pi}\cos\left(\frac{2}{3}(-s)^{3/2} - \frac{\pi}{4}\right)}{(-s)^{3/4}} + \log(-s)\right) + D_4, \tag{76}$$

where the notation $\delta\Phi^{\leftarrow}$ refers to a solution to the left of the upper hybrid radius, as in Fig. 6. We can read off the fluid and Bernstein solutions by separating oscillatory dependence from the logarithmic divergence. By comparing this expression to Eq. (25), one can see that the fluid component on the left side of the upper hybrid radius is

$$\overline{\delta\Phi}^{\leftarrow}(s) = D_3\log(-s) + D_4. \tag{77}$$

To the right of the upper hybrid radius, the asymptotic form requires that the Airy solution in Eq. (73) be integrated with the same constant of integration as was obtained in Eq. (76). To ensure this is the case, use is made of the identities $\int_{-\infty}^{\infty}\mathrm{Ai}(s)\,ds = 1$ and $\lim_{N\to\infty}\int_{-N}^{N}\mathrm{Ci}(s)\,ds = 0$. Once the evanescent Bernstein solution dies away, we are left with the outer fluid solution which now takes the form

$$\overline{\delta\Phi}^{\rightarrow}(s) = D_1 + D_4 + D_3\log(s). \tag{78}$$

Note that in Eqs. (77) and (78), s can be replaced by $r - r_{\mathrm{UH}}$ since the multiplicative factor relating $r - r_{\mathrm{UH}}$ and s implies that $\log(\pm s)$ equals $\log(\pm(r - r_{\mathrm{UH}}))$ plus an additive constant that can be absorbed into D_4

$$\overline{\delta\Phi}^{\leftarrow}(r) = D_3\log(r_{\mathrm{UH}} - r) + D_4, \tag{79}$$

$$\overline{\delta\Phi}^{\rightarrow}(r) = D_1 + D_4 + D_3\log(r - r_{\mathrm{UH}}). \tag{80}$$

These results agree in form with the fluid theory near r_{UH} from Eqs. (25) and (28). However, the additive constant D_1 appears as an amplitude in the oscillatory Bernstein solution. The Bernstein wave couples to the fluid solution, modifying it at the radius r_{UH}, and introducing a jump in the form of the fluid solution across the transition region, due to the Bernstein wave coupling.

F. Matching solutions across r_{UH}

Evaluating Eqs. (79) and (80) at r_{UH_0}, and recalling from Eq. (24) the definition $i\Delta r \equiv r_{\mathrm{UH}} - r_{\mathrm{UH}_0}$, we have

$$\begin{aligned} &\overline{\delta\Phi}^{\leftarrow}(r_{\mathrm{UH}_0}) = D_3\log(i\Delta r) + D_4, \quad \overline{\delta\Phi}^{\leftarrow\prime}(r_{\mathrm{UH}_0}) = -D_3/i\Delta r, \\ &\overline{\delta\Phi}^{\rightarrow}(r_{\mathrm{UH}_0}) = D_3\log(-i\Delta r) + D_1 + D_4, \\ &\overline{\delta\Phi}^{\rightarrow\prime}(r_{\mathrm{UH}_0}) = -D_3/i\Delta r. \end{aligned} \tag{81}$$

Note that $\Delta r < 0$ according to Eq. (23) because, for the case of interest here, ϵ_{11} is a monotonically increasing function of radius [see the discussion following Eq. (58)].

We can match the oscillatory part of $\delta\Phi^{\leftarrow}$ to $\widetilde{\delta\Phi}_{\mathrm{WKB}}$ by comparing Eqs. (66)–(76). To do this, keep in mind that k is linked with the dielectric through Eq. (58), which as we approach $r = r_{\mathrm{UH}}$ (where ϵ_{11} is evaluated close enough to the upper-hybrid radius that it varies linearly in r), becomes

$$k = \sqrt{\frac{r_{\mathrm{UH}} - r}{r_c^2\mathcal{L}}}. \tag{82}$$

Now use this to determine the integral in Eq. (66)

$$\int_{r_{\mathrm{UH}}}^{r} k(\bar{r})\,d\bar{r} = \frac{-2}{3r_c\sqrt{\mathcal{L}}}(r_{\mathrm{UH}} - r)^{3/2} = -\frac{2}{3}(-s)^{3/2}. \tag{83}$$

This result can be used to replace the argument of the cosine and sine functions in Eq. (76) with integrals over $k(r)$,

allowing us to match this result to the WKB eikonal form of Eq. (66). Using Eq. (67), the matching requires that

$$\tan\left(\chi-\frac{\pi}{4}\right)=\frac{D_1}{\pi D_3}. \tag{84}$$

We can then use this expression to solve for D_1 and apply this in Eq. (81) to obtain jump conditions matching the inner and outer fluid solutions across transition region.

As shown in Fig. 8, we can express $\log(-x)=\log(x)-i\pi$, for all x on the left half of the red line when Δr is negative. Then, we can use Eq. (81) to relate $\delta\Phi^{\leftarrow}$ and $\delta\Phi^{\rightarrow}$ via the jump conditions

$$\begin{aligned}\overline{\delta\Phi}^{\rightarrow\prime}(r_{\mathrm{UH}_0})&=\overline{\delta\Phi}^{\leftarrow\prime}(r_{\mathrm{UH}_0}),\\ \overline{\delta\Phi}^{\rightarrow}(r_{\mathrm{UH}_0})&=\overline{\delta\Phi}^{\leftarrow}(r_{\mathrm{UH}_0})\\ &\quad-i\Delta r\,\pi\,\overline{\delta\Phi}^{\leftarrow\prime}(r_{\mathrm{UH}_0})\left(\tan\left(\chi-\frac{\pi}{4}\right)+i\right).\end{aligned} \tag{85}$$

For clarity, it should be noted that the choice of r_{UH0} in Eq. (85) is merely a convenience. Equation (85) could also be evaluated at any other point r within the transition region near r_{UH}, with the substitution $i\Delta r=r_{\mathrm{UH}}-r$. This relies on the fact that the functional forms of the fluid solutions, Eqs. (79) and (80), are both valid solutions of the fluid theory ODE Eq. (25) in the transition region, each matching onto the numerical fluid solutions on their respective side of the upper hybrid radius.

In a similar vein, it is informative to consider what is going on with the jump conditions Eq. (85) as $\nu\to 0$. It appears that the last term in the second condition vanishes as $\nu\to 0$, because Δr is proportional to ν [see Eq. (23)]. However, Eq. (81) implies that $\Delta r\overline{\delta\Phi}^{\leftarrow\prime}(r_{\mathrm{UH0}})$ is independent of Δr as $\Delta r\to 0$, so the last term in the jump condition remains finite as $\nu\to 0$.

These jump conditions provide results for the potential that are correct to $O((\Delta r/\mathcal{L})^0)$, neglecting corrections that are proportional to higher powers of $\Delta r/\mathcal{L}$. This is because the conditions rely on low-order asymptotic forms for the fluid potential in the transition region, Eqs. (79) and (80), which are correct only up to and including order $(r-r_{\mathrm{UH}})^0$.

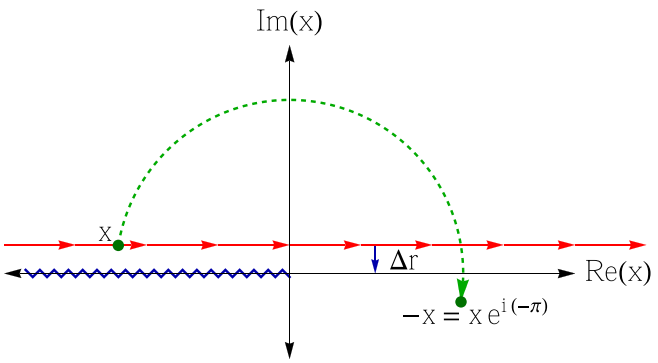

FIG. 8. Complex plot of $x=r-r_{\mathrm{UH}}$. The real r axis is the red line (noting that Δr is negative). The dashed green contour relates x to $-x$ while avoiding the branch cut (blue zig-zag).

As a consequence, the conditions are only useful provided that $\Delta r/\mathcal{L}\ll 1$.

We can now integrate the fluid theory Eq. (6) numerically from $r=0$ to r_w, using the jump conditions Eq. (85) to continue integration across the upper-hybrid cutoff. Here, χ is evaluated using Eq. (67). This result gives the fluid theory solution everywhere. Recalling how the perturbed potential can be expressed as a sum of a fluid theory solution and a Bernstein wave solution via Eq. (63), and also noting that the Bernstein wave solution is evanescent outside the upper hybrid radius, we can calculate the admittance $Y(\omega)$ by using Eq. (29), replacing $\delta\Phi\to\overline{\delta\Phi}$. That is,

$$Y=\left.\frac{r_W\dfrac{\partial\overline{\delta\Phi}}{\partial r}}{\overline{\delta\Phi}}\right|_{r=r_W}. \tag{86}$$

The value of χ in Eq. (85) is obtained using Eq. (67) by integrating over $k(r)$ numerically from $r=0$ up to $r=r_{0\mathrm{UH}}$, assuming that ν is small so that the difference Δr between r_{UH} and $r_{0\mathrm{UH}}$ can be neglected. For given ω, the function $k(r)$ is obtained by solving the dispersion relation, Eq. (58).

As another check of the jump conditions, in the cold plasma limit (i.e., as $r_c\to 0$) the argument of the tan function in Eq. (85) picks up a large negative imaginary part due to the influence of collisions on $k(r)$, and so $\tan(\chi-\pi/4)+i\to 0$. Then, there is no-longer a jump in the fluid theory solution across the upper hybrid radius; in other words, the fluid theory ODE can be integrated without change from the plasma interior to the wall, resulting in the same cold fluid admittance function $Y(\omega)$ as obtained previously.

As a final check, we compare the Bernstein mode frequencies obtained from Eq. (85) in the large magnetic field limit to a result in Ref. 1. In the large-field limit, the fluid potential for $r<r_{\mathrm{UH0}}$ is given by Eq. (12) with B chosen so that the solution is finite at $r=0$:

$$\overline{\delta\Phi}^{\leftarrow}=Ar^{-\ell}\int_0^r dr'\frac{r'^{(2\ell-1)}}{D(r')}, \tag{87}$$

where A is an undetermined coefficient. Similarly, using Eq. (12) to match the outer potential to the potential at the wall yields

$$\overline{\delta\Phi}^{\rightarrow}=\delta\Phi_W(r_W/r)^{\ell}+Cr^{-\ell}\int_r^{r_W} dr'\frac{r'^{(2\ell-1)}}{D(r')}, \tag{88}$$

where C is a different undetermined coefficient. Applying these forms to the jump conditions allows us to determine the coefficients A and C. The solutions are simplified by keeping only terms of order Δr^0 and noting that $D(r_{\mathrm{UH0}})\approx -i\Delta r/\mathcal{L}$. We find that the first condition implies that $A=-C+O(\Delta r)$ and using this in the second condition yields

$$C\left(\int_0^{r_W} dr'\frac{r'^{(2\ell-1)}}{D(r')}+\pi\mathcal{L}r_{\mathrm{UH0}}^{2\ell-1}(\tan[\chi-\pi/4]+i)\right)=-\delta\Phi_W r_W^{\ell}. \tag{89}$$

Bernstein modes occur at frequencies for which the coefficient of C vanishes. This condition can be rewritten as

$$\chi = \frac{\pi}{4} + n\pi + \arctan\frac{r_{\mathrm{UH0}}^{1-2\ell}}{\pi\mathcal{L}}\left(-\int_0^{r_W} dr' \frac{r'^{(2\ell-1)}}{D(r')} - i\pi\mathcal{L}r_{\mathrm{UH0}}^{2\ell-1}\right), \tag{90}$$

where n is any integer and the main branch of the arctan function is taken. Using Eq. (67) and noting that, for small $\Delta r/\mathcal{L}$, the Plemelj formula can be applied to integrate past the pole in the integral over $1/D(r')$, we obtain

$$\int_0^{r_{\mathrm{UH0}}} k dr = \frac{(\ell+1)\pi}{2} + n\pi - \arctan\left(\frac{r_{\mathrm{UH0}}^{1-2\ell}}{\pi\mathcal{L}}\mathcal{P}\int_0^{r_W} d\bar{r}\frac{\bar{r}^{(2\ell-1)}}{D(\bar{r})}\right), \tag{91}$$

where $\mathcal{P}$ indicates that the principal part of the integral is taken. This expression for the Bernstein mode dispersion relation in the large field limit agrees with Eq. (152) in Ref. 1 (with a redefinition of the integer n to $n-1$).

VI. VLASOV vs. NEW WKB AND OLD WKB THEORIES

We now present the results of the new WKB theory for various magnetic fields, values of ℓ, and density profiles, comparing the theory to numerical solutions of the Vlasov equation and to the prior large magnetic field WKB theory.[1]

We first study a $\ell = 4$ perturbation in a plasma with $r_p = 4.76, r_W = 10, \Omega = 5$, and $\nu = 1/300$. These parameters are similar to a case studied by Dubin. In Fig. 9, we compare the new WKB solution for the admittance to the Vlasov numerical method and to the prior WKB theory.[1]

The new WKB theory produces a mode frequency prediction that is closer to the Vlasov solution than the old WKB theory. Again, the shift in the frequency between the old and new theories arises from the large magnetic field approximation for the cold-fluid dielectric that was used in the old theory. Also, both WKB theories have a slight, but consistent overestimation of the admittance. This is probably related to finite temperature corrections to the cold fluid theory that are neglected in the WKB approach used here.

In the next figures, we vary the magnetic field strength. In Fig. 10, we vary Ω from 4 to 10 for an $\ell = 4$ perturbation, and in Fig. 11, we do the same for an $\ell = 2$ perturbation. For a given peak (corresponding to the number of radial nodes in the wave), the relative error in the scaled mode frequency λ tends to decrease as magnetic field increases from $\Omega = 4$ to

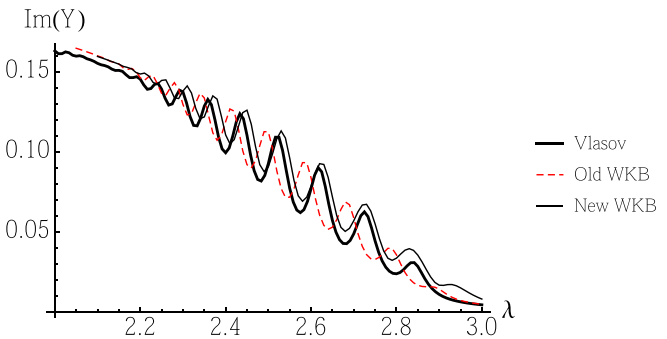

FIG. 9. Comparison of Vlasov and WKB approximations, for $\Omega = 5$, $r_p = 4.76$, $r_W = 10$, $\ell = 4$, and $\nu = 1/300$. Vlasov code uses M_ψ=8, $M_r = M_v = 120$.

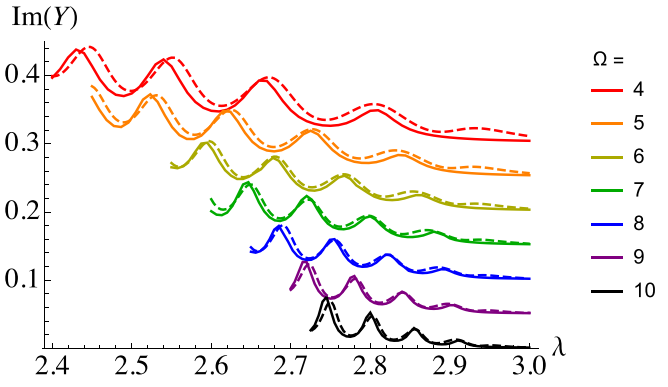

FIG. 10. A family of Admittance plots (solid: Vlasov theory; dashed: New WKB theory). $r_p = 4.76$, $r_W = 10$, and $\ell = 4$. $1/\nu = 2000 \times 2^{\frac{\Omega-10}{2}}$ (traces shifted vertically in steps of 1/20, with $\Omega = 10$ trace unshifted).

$\Omega = 10$. (This is easiest to see in the second and third peaks, counting from the right). This is because the criterion for WKB theory to be valid is $k'(r)/k \ll k$ and k increases as magnetic field increases. This WKB criterion can also be written as $k\mathcal{L} \gg 1$ since $k/k' \approx \mathcal{L}$.

Interestingly, for a given magnetic field strength the figures show that the WKB method tends to produce more accurate results toward the right side of the plots, for larger frequencies and therefore *smaller* k (although the WKB theory tends to predict a weak extra peak at the largest frequencies and for smaller magnetic fields). This can be understood because k'/k also varies as the frequency varies. As the frequency drops, k'/k becomes larger because the upper hybrid radius shifts to a larger radius where the density profile is steeper. A second reason for the increase in k'/k at lower frequencies is the appearance of wave-particle resonances. These resonances occur at radii r_{wpr} where the dielectric constant ϵ_{11} diverges. According to Eq. (7), the divergences occurs where $\hat{\omega}^2 - \Omega_v(\Omega_v - r\omega_f') = 0$. Around such locations there is a strong resonant interaction between the wave electric field and particle cyclotron motion, which causes Landau damping of the wave. WKB theory breaks down here because as ϵ_{11} diverges k' also diverges. In Fig. 12, we plot the WKB criterion $k_0\mathcal{L}_{min}$ versus frequency, where $\mathcal{L}_{min} = \min[\mathrm{Re}(\epsilon_{11}/\epsilon_{11}'(r))]$ is the minimum gradient scale length across the radial profile and $k_0 = \mathrm{Re}[k(r=0)]$ is the

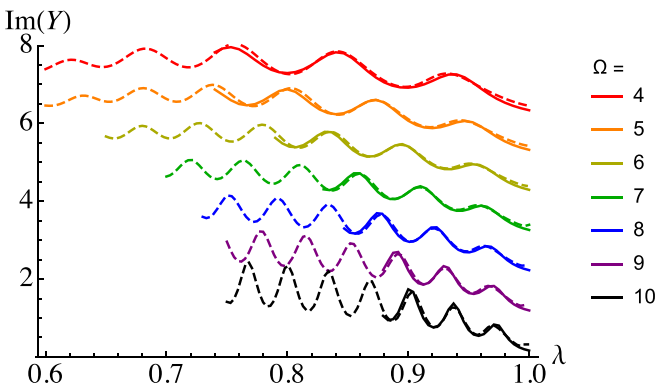

FIG. 11. A family of Admittance plots (solid: Vlasov theory; dashed: New WKB theory). $r_p = 4.76$, $r_W = 10$, and $\ell = 2$. $1/\nu = 2000 \times 2^{\frac{\Omega-10}{2}}$ (traces shifted vertically in steps of 1, with $\Omega = 10$ trace unshifted).

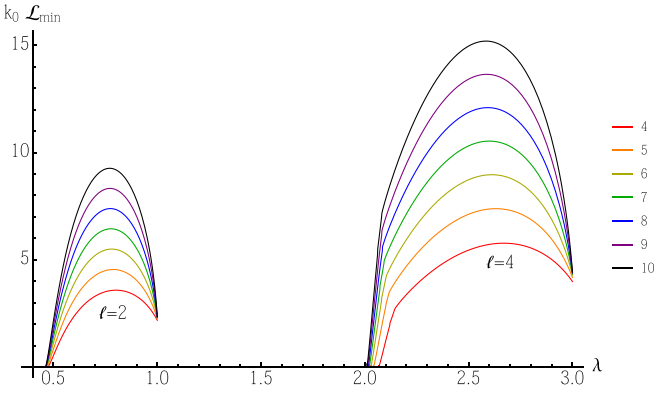

FIG. 12. The WKB parameter $k_0\mathcal{L}_{min}$ plotted versus scaled frequency λ for a range of magnetic fields and for both $\ell=2$ (left) and $\ell=4$ (right), for the waves and magnetic fields considered in Figs. 10 and 11. WKB theory works best when $k_0\mathcal{L}_{min} \gg 1$.

real part of the central wavenumber. The WKB convergence parameter $k_0\mathcal{L}_{min}$ approaches zero at the first appearance of a wave-particle resonance in the plasma, which occurs at frequencies on the left side of the plots for $\ell=2$ and $\ell=4$. The WKB parameter also decreases at higher frequencies, to the right side of the plots where the wavenumber of the modes is smaller. Consequently, the WKB method should work best at intermediate values of the frequency (and, of course, at larger magnetic fields). This expected behavior roughly corresponds to the results shown in Figs. 9–11.

VII. LIMITING FORM FOR THE MODE FREQUENCIES

It would be useful to have an analytical expression to approximate the Bernstein Mode frequencies without having to numerically solve the fluid theory solution and impose a jump condition at r_{UH}. In this regard, the analytical large magnetic field dispersion relation used in the old WKB theory, Eq. (91), is useful. A significant simplification can be made in the limit where the wall radius is large, $r_w/r_p \to \infty$. In this case, the argument of the arctan function in Eq. (91) approaches infinity. For instance, in the former limit, the Cauchy Principal integral is dominated by the vacuum region where $\mathcal{D} \to 1$, and the integrand grows without bound as a simple power law. Consequently, the argument of the arctan term approaches $\pi/2$. Making this approximation, Eq. (91) can be simplified to read

$$\int_0^{r_{UH}} k dr = \left(\frac{\ell}{2} + n\right)\pi. \tag{92}$$

Although this result was obtained from the large magnetic field limit of the theory, it no-longer depends on the large-field fluid solution and so we might hope that it is more generally correct. We will test this hypothesis below. First, however, to standardize the integer n so that n indexes the modes starting from 1, we impose the constraint that the integral in Eq. (92) must be strictly positive, since $k>0$ for $0<r<r_{UH}$. The issue is that $\ell/2$ term can be larger than 1, meaning that subtracting 1 from $n=1$ (the lowest solution, by definition) would still produce a strictly positive right-hand side solution, which is not what we want. To solve this, we redefine n to absorb the largest integer that is still strictly less than $\ell/2$. The effect is that the right-hand side reads $n\pi$ when ℓ is even, and $(n-1/2)\pi$ when ℓ is odd

$$\int_0^{r_{UH}} k dr = (n + \mathrm{mod}(\ell,2)/2)\pi. \tag{93}$$

Again, Eq. (93) assumes that r_w/r_p is large. The functions $k(r)$ and r_{UH} must be calculated exactly using Eq. (57) as a function of the driving frequency. This result is similar to a result in Ref. 1, where instead the limit $\mathcal{L}/r_{UH} \ll 1$ was assumed; i.e., a nearly square density profile. While we tried assuming a square profile with upper hybrid radius equal to the plasma radius by writing $\int_0^{r_{UH}} k dr \approx k(0) r_p$, this completely misrepresents the lowest-order modes because r_{UH} actually increases from zero quite rapidly for the first few modes due to the non-rectangular profile. Unfortunately, correct determination of Bernstein mode frequencies is strongly dependent on the assumed plasma profile. To understand this strong dependence, we can think of the right-hand side of Eq. (93) (divided by π) as counting the number of half-wavelengths within a radius r_{UH}. For the low-order modes, r_{UH} is very sensitive to the profile shape in the nearly uniform region of the plasma [since even a small variation in the falloff of $k(r)$ corresponds to a large variation of r_{UH} due to the small gradient of $k(r)$]. Consequently, even if $k(r)$ were known precisely, the number of half-wavelengths within this variable r_{UH} is also variable. On the other hand, for higher order modes, while r_{UH} is less sensitive to the profile shape (since r_{UH} falls somewhere in the relatively thin plasma edge), $k(r)$ is larger, so even a small variation in r_{UH} admits a larger variation in the number of allowable half-wavelengths. In Fig. 13, the new WKB theory peaks are plotted against the prediction of the mode frequencies for an infinite wall radius via Eq. (93). As can be seen, the mode frequencies are very well predicted by Eq. (93) for the infinite wall radius, even for a warm plasma that doesn't satisfy $r_{UH} \gg \mathcal{L}$.

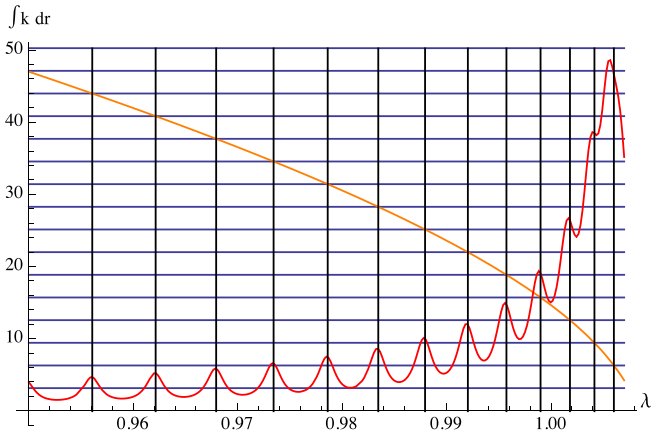

FIG. 13. Determination of mode frequencies from Eq. (93). Orange curve: $\int_0^{r_{UH}} k\,dr$, horizontal lines: $(n+\mathrm{mod}(\ell,2)/2)\pi$, vertical lines: intersection of orange curve with horizontal blue lines, red peaks: ImY from the new WKB theory multiplied by $(r_W/r_p)^{2\ell}$ (scaled vertically to fit). $\Omega=10$, $R_p=20, \ell=2, r_w/r_p=\infty$.

VIII. EXTENSION TO MULTIPLE SPECIES

The analysis of Secs. IV and V can be extended to a multi-species plasma in a straightforward way. We make the assumption that the plasma is warm enough to not be centrifugally separated, which is done both as a simplifying assumption for the theory and for comparing to experiments that operate in this regime, where Bernstein modes are more easily observed.

A. Resonant species approximation with no species separation

If the plasma species are not centrifugally separated, the densities of each species are related according to

$$n_\alpha(r) = \delta_\alpha n_{\rm tot}(r),\ \alpha = 1, 2, \ldots n,$$

where $\delta_\alpha = n_\alpha(0)/n_{\rm tot}(0)$ is the central species concentration of species α. Consequently, knowledge of $n_{\rm tot}$, along with the species fractions, is sufficient to determine the equilibrium for each species individually. To calculate this equilibrium, we note that under the approximation that the species are not centrifugally separated, the total unperturbed density $n_{\rm tot}$ behaves as a single species, so the equilibrium Eq. (2) still holds, where all quantities are normalized to the central parameters associated with the total plasma.

Then, the multi-species generalization of the local WKB dispersion function Eq. (58) is

$$\mathcal{D}(\omega, k, r) = 1 - 2\sum_\alpha X_\alpha(\omega, r)\frac{e^{-\Lambda_\alpha} I_1(\Lambda_\alpha)}{\Lambda_\alpha}, \tag{94}$$

where $\Lambda_\alpha = k^2 r_{c\alpha}^2$ and X_α can be written as

$$X_\alpha(\omega, r) = \frac{\omega_{p\alpha}^2}{\hat{\omega}^2 - \Omega_{v\alpha}(\Omega_{v\alpha} - r\omega_f')}. \tag{95}$$

Here, $\Omega_{v\alpha} = \Omega_\alpha - 2\omega_f$, and Ω_α, $\omega_{p\alpha}$, and $r_{c\alpha}$ are the cyclotron frequency, plasma frequency, and cyclotron radius of species α, respectively. As in Eq. (58), we have dropped resonant terms at multiples of the cyclotron frequency for each species, since we are interested in the main resonance at the fundamental cyclotron frequency. There will then be a solution of the dispersion relation $\mathcal{D} = 0$ for each species; i.e., each species has a cyclotron wave associated with it.

In order to make further progress, we will simplify this result assuming that the magnetic field is large. In this case, we know that the plasma response is peaked in a narrow frequency range around the cyclotron frequency for each species, with $\omega - \Omega_\alpha \approx \omega_{p\alpha}^2/\Omega_\alpha$. We assume that the magnetic field is large enough so that this range is small compared to the difference between any two cyclotron frequencies: $\Omega_\alpha - \Omega_\beta \gg \omega_p^2/\Omega$. In this case, for cyclotron waves associated with a given species β with $\omega \approx \Omega_\beta$, only the resonant term with $\alpha = \beta$ needs to be kept in the sum in Eq. (94) because $X_\alpha \ll X_\beta$, and the equation simplifies to

$$\mathcal{D}(\omega, k) = 1 - 2X_\beta(\omega)\frac{e^{-\Lambda_\beta} I_1(\Lambda_\beta)}{\Lambda_\beta}. \tag{96}$$

In other words, in this approximation we ignore the response of all non-resonant species. In this case, the WKB theory carries through just as for a single species (the resonant species). Also, this approximation can easily be applied to the numerical Vlasov solution. Here, all species contribute to the equilibrium electric field appearing in Eq. (33), but δf is evaluated only for the resonant species.

B. Necessary conditions for Bernstein modes

An important question to consider is "Under what conditions are Bernstein modes possible in a multi-species thermal equilibrium plasma?". As previously discussed for a single-species plasma, Bernstein waves can only propagate when $\mathrm{Re}(\epsilon_{11}) < 0$. For a multi-species plasma in the resonant species approximation, this corresponds to $X_\beta > 1$ for resonant species β. There is a range of frequencies near Ω_β where this inequality is satisfied. To find this range, we utilize the high magnetic field limiting form of X_β

$$X_\beta = \frac{\delta_\beta \cdot n}{\lambda + (2-\ell)\langle n\rangle + \dfrac{r\langle n\rangle'}{2}} = \frac{\delta_\beta \cdot n}{\lambda + (1-\ell)\langle n\rangle + n}, \tag{97}$$

where n is the total density scaled to the total density at $r = 0$, $\lambda \equiv \frac{\omega - \Omega_\beta}{\omega_E}$, $\omega_E = 2\pi e c n(r=0)/B$ is the central E × B rotation rate, $\langle n\rangle$ is the average total density within a radius r, and δ_β is the fraction of the mode resonant species β. The final expression follows by carrying out the radial derivative of $\langle n\rangle$. The expression in Eq. (97) is useful because it allows insight into where both the cutoffs and wave-particle resonances occur

$$\lambda = (\ell - 1)\langle n\rangle_r - (1 - \delta_\beta)\, n(r) \quad \text{(cutoff)}, \tag{98}$$

$$\lambda = (\ell - 1)\langle n\rangle_r - n(r) \quad \text{(resonance)}. \tag{99}$$

At the cutoff, $Re[X_\beta] = 1$ ($Re[\epsilon_{11}] = 0$) while at the wave-particle-resonance, $X_\beta \to \infty$. A cutoff is typically required in order for propagating solutions to exist because $\epsilon_{11} = 1$ outside the plasma but $Re[\epsilon_{11}] < 0$ is necessary for wave propagation. Another way for ϵ_{11} to change sign is to go through infinity, at a wave-particle-resonance (WPR). However, a wave-particle resonance in the plasma strongly Landau-damps the Bernstein waves, so we look for conditions where the plasma has a cutoff but no resonance. For $\ell = 0$ or $\ell = 1$, Eqs. (98) and (99) imply that a cutoff is always accompanied by a resonance at a somewhat larger radius, so the Bernstein response is heavily damped. However, for $\ell > 1$ one can find a frequency range with a cutoff but no resonance. The right-hand sides of Eqs. (98) and (99) are functions of r and have maximum values as a function of r. Note that the maximum value for the wave particle resonance condition is clearly less than that for the cutoff condition.

Thus, for Bernstein modes to occur, λ must be less than the maximum value given by Eq. (98) but greater than the maximum given by Eq. (99): $\lambda_{\rm wpr} < \lambda < \lambda_{\rm cut}$ where

$$\lambda_{\rm cut} = \max\big((\ell-1)\langle n\rangle_r - (1-\delta_\beta)\, n(r)\big), \tag{100}$$

$$\lambda_{\rm wpr} = \max\big((\ell-1)\langle n\rangle_r - n(r)\big), \tag{101}$$

and where max() is the global maximum operator as r varies. Notice that the wave-particle resonance does not depend on δ_β because δ_β does not appear in the denominator of X_β. In fact,

$$\lambda_{\rm wpr} = \lambda_{\rm cut}|_{\delta_\beta\to 0}. \tag{102}$$

Consequently, plasmas with a small fraction δ_β of the resonant species exhibit Bernstein modes only over a narrow range of frequencies, so future experiments on Bernstein modes should strive to make the resonant species fraction as large as possible.

The next task is to understand the dependence of $\lambda_{\rm cut}$ and $\lambda_{\rm wpr}$ on the remaining parameters of the plasma, δ_β, r_p, and ℓ. In Fig. 14, it is clear that the Bernstein range in λ satisfies $\ell-2<\lambda<\ell-1$, with warmer (i.e., smaller r_p) plasmas extending through that entire range, except for $\ell=2$, which first acquires a wave-particle resonance at a higher frequency than $\lambda=\ell-2=0$. It is also interesting to note that in the case of $\ell=4$, the bottom limit of $\omega_{\rm wpr}$ becomes constant at sufficiently small r_p due to the appearance of a second wave-particle resonance that first appears at the very center of the plasma, at a higher frequency than the wave-particle resonance appearing at non-zero r. The kinks in the curves for $\lambda_{\rm cut}$ at various δ_β show whether the region in which there are Bernstein wave solutions is a disk-shaped region or an annular region. That is, for sufficiently large r_p, the plasma has two upper hybrid radii. These annular solutions only occur for $\delta_\beta<1$.

To understand the fluid theory in a concrete situation, we now study a particular plasma with parameters chosen to match some typical experimental conditions. Figure 15 shows several traces of $\epsilon_{11}(r)=1-X_\beta$ for a range of driving frequencies. The red (dotted) curve shows the lowest

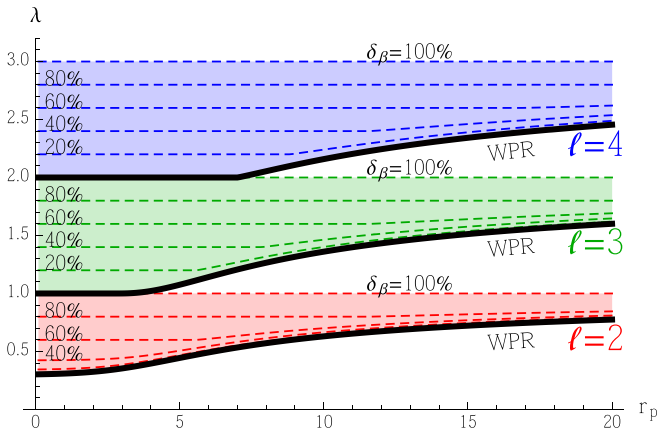

FIG. 14. Predicted ranges of λ over which Bernstein modes occur in WKB theory for a multispecies plasma without species separation: $\lambda_{wpr}<\lambda<\lambda_{cut}$, as a function of scaled plasma radius for $\ell=2$ through $\ell=4$, with resonant species fraction $\delta_\beta\in\{100\%,80\%,60\%,40\%,20\%\}$. Here, λ_{cut} is shown as dashed curves for the different species fractions, and λ_{wpr} is shown as the thick solid lines. The plasma response for $\ell\le 1$ does not exhibit Bernstein modes in WKB theory.

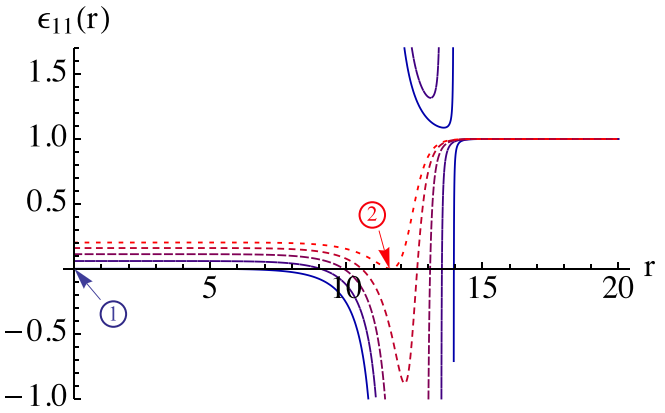

FIG. 15. $\epsilon_{11}(r)$ in a plasma with $\ell=2$, $\Omega=10.45$, $r_p=10.5$, $\delta_\beta=56.3\%$, $r_w=83.54$, with driving frequencies starting from $\lambda=0.711$ (red, dotted), down to $\lambda=0.568$ (blue, solid). Locations where $\epsilon_{11}(r)=\epsilon'_{11}(r)=0$ labeled.

frequency for which some part of the plasma has $\epsilon_{11}<0$ for $\nu=0$, due to the dip in ϵ_{11} at roughly $r=11.5$. This frequency is how we defined $\lambda_{\rm cut}$, as shown by the dashed lines in Fig. 14. In this case, $\epsilon_{11}<0$ only in a small region away from the origin, that is, this plasma exhibits Bernstein modes in an annular region, with evanescence both near the plasma center, and at the very edge of the plasma. As the driving frequency is lowered further, the dip in ϵ_{11} becomes increasingly deep until at some frequency $\lambda_{\rm wpr}$ the denominator appearing in ϵ_{11} vanishes and two wave-particle resonances are produced that damp out the Bernstein waves, as indicated by the thick black lines in Fig. 14.

C. Multi-species results

In Fig. 16, we compare the multi-species results of the WKB theory for $\ell=2$ modes in an $\Omega=10$, $r_p=4.76$ plasma, with two values of the resonant species purities δ_β, using the resonant-species approximation discussed previously. First, we take $\delta_\beta=80\%$. Notice that the right side of Fig. 16 is at $\lambda=0.8$, in agreement with the prediction by Fig. 14, since no Bernstein peaks appear at frequencies

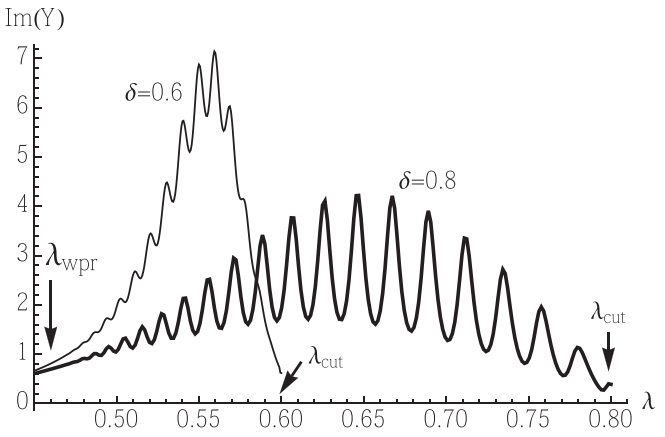

FIG. 16. Imaginary part of the admittance for a multi-species plasma, using the WKB theory, for two resonant species fractions, $\delta_\beta=60\%$ and 80%. $\Omega=10$, $r_p=4.76$, $r_W=10$, $\ell=2$ and $1/\nu=4000$. Compare the fall-off of the response to the predictions for λ_{wpr} and $\lambda_{\rm cut}$ provided by Fig. 14 (arrows).

higher than this according to WKB theory. There appears to be a significant reduction in peak spacing compared to the pure plasma case (Fig. 11).

Next we consider an identical plasma except with $\delta_\beta = 60\%$. Again, the plot starts on the left at $\lambda = 0.6$, as expected from the appearance there of an $\ell = 2$ wave-particle resonance in this profile shown in Fig. 14. We also observe that the Bernstein peaks are more difficult to observe in a $\delta_\beta = 60\%$ plasma, especially for frequencies approaching λ_{cut} than it was for the $\delta_\beta = 80\%$ plasma. This is because the peak spacing is even closer together in the $\delta_\beta = 60\%$ plasma.

D. ℓ=0 Bernstein modes

We now briefly consider excitation and measurement of the $\ell = 0$ plasma response to an external perturbation near the cyclotron frequency and compare these results to simulations by Hart and Spencer of $\ell = 0$ cyclotron waves.[6] There are two ways in which the $\ell = 0$ plasma response differs from the $\ell \neq 0$ response discussed previously.

First, for $\ell = 0$ a wave-particle resonance occurs that strongly damps Bernstein modes. Although previously we argued that Bernstein waves are completely absorbed at a wave-particle resonance, we will see that sometimes a weak Bernstein mode can still be set up. When the resonant radius occurs in the region of the plasma edge, and if this edge density falls rapidly to zero, a new effect occurs: Bernstein waves are partially reflected at the sharp plasma boundary rather than being completely absorbed, creating a damped standing wave inside the plasma. This is an effect beyond WKB theory. We therefore rely on numerical Vlasov solutions, comparing them to the predictions of cold fluid theory (which does not include the Bernstein response at all), and to the particle simulations of Hart and Spencer.

Second, we cannot drive an $\ell = 0$ plasma wave using an external wall potential, since a cylindrically symmetric $z-$ independent wall potential does not create a radial electric field for $r < r_W$. Also, $\ell = 0$ plasma oscillations cannot be detected at the wall, by Gauss's law in two-dimensions. (Experimentally, there can be z-dependence in the driver, and the plasma is finite-length, but such effects are beyond the two-dimensional theory presented here). We therefore must drive the plasma in a different manner than for $\ell \neq 0$ and we must diagnose the modes using a new definition of plasma admittance.

We will drive the plasma with an oscillatory θ-independent potential of the form $\delta\Phi_{ext}(r)e^{-i\omega t}$, where $\delta\Phi_{ext}(r)$ does *not* satisfy the 2-D Laplace equation; instead we simply take $\delta\Phi_{ext}(r) = Ar^2$. One can think of this as some approximation to the effective 2-D (z-averaged) driving one would obtain in a finite-length plasma from a z-dependent wall voltage.

Next, we require a new form for the admittance function. Hart and Spencer define their measure of the $\ell = 0$ plasma response as the amplitude of the radial component of the fluid velocity, δV_r, at a fixed location on the interior of the plasma, r_{meas}. We will use a related dimensionless quantity we call Y_a, the "acceleration admittance," defined as the (negative of) the radial acceleration of a fluid element at a given location r_{meas}, divided by the acceleration produced by the external potential only

$$Y_a \equiv -\left.\frac{i\omega\delta V_r}{\partial\delta\Phi_{ext}/\partial r}\right|_{r=r_{meas}}. \tag{103}$$

Like the admittance Y, the quantity Y_a is independent of the amplitude A of the external driving potential; its imaginary part depends only on the plasma response; and it is sharply peaked at the frequencies of weakly damped normal modes.

There are (at least!) two ways to determine this admittance function from the Vlasov solution. In one method, one can integrate the numerically determined distribution function δf over velocities to determine δV_r and use this result in Eq. (103). Another, simpler method uses a relation between δV_r and the perturbed plasma potential, $\delta\Phi_p$. To derive this relation, begin with the linearized continuity equation

$$-i\omega\delta n + \nabla\cdot\left(n\delta\mathbf{V} + \delta n\mathbf{V}_f\right) = 0, \tag{104}$$

where $\mathbf{V}_f(r) = \omega_f(r)r\hat{\theta}$ is the equilibrium cold-fluid rotational velocity and $n(r)$ is the equilibrium density [see Eqs. (1) and (9)]. Integrating this equation over a disk of radius r centered with the plasma and using the divergence theorem, we obtain

$$\oint n\delta\mathbf{V}\cdot\hat{n}ds + \oint\delta n\mathbf{V}_f\cdot\hat{n}ds = \int i\omega\delta n d^2r. \tag{105}$$

The second term on the left vanishes due to the purely azimuthal equilibrium flow. Using the Poisson equation

$$\nabla^2\delta\Phi_p = -\delta n, \tag{106}$$

another application of the divergence theorem, and cylindrical symmetry for $\ell = 0$, the right side of Eq. (105) can be expressed in terms of the radial plasma electric field, which gives the following expression for the perturbed radial velocity for an $\ell = 0$ plasma:

$$\delta V_r(r) = -\frac{i\omega}{n(r)}\frac{\partial\delta\Phi_p}{\partial r}. \tag{107}$$

We will use this result in Eq. (103) to determine the plasma response to an external potential oscillation for $\ell = 0$ using the Vlasov code. We will also compare these numerical Vlasov code results to the predictions of cold fluid theory. However, since the driving potential does not satisfy the Laplace equation, the cold fluid theory of Eq. (6) must be modified. The linearized cold fluid equations from which it is derived are the continuity and Poisson equations Eqs. (104) and (106), as well as the linearized momentum equation,

$$\begin{aligned}-i\omega\delta\mathbf{V} + \mathbf{V}_\mathrm{f}\cdot\nabla\delta\mathbf{V} + \delta\mathbf{V}\cdot\nabla\mathbf{V}_\mathrm{f}\\ = -\nabla\delta\Phi_p - \nabla\delta\Phi_{ext} - \Omega\delta\mathbf{V}\times\hat{z}.\end{aligned} \tag{108}$$

These three equations can be combined to yield

$$\nabla\cdot\epsilon\cdot\nabla\delta\Phi_p = \nabla\cdot(1-\boldsymbol{\epsilon})\cdot\nabla\delta\Phi_{ext}, \tag{109}$$

where ϵ is the cold-fluid dielectric tensor given by Eq. (7). This is a generalization of Eq. (6) to forcing potentials that do not satisfy the 2-d Laplace equation. If $\delta\Phi_{ext}$ did satisfy the Laplace equation, it could be combined with the plasma potential $\delta\Phi_p$ as $\delta\Phi = \delta\Phi_p + \delta\Phi_{ext}$ and $\delta\Phi$ would satisfy Eq. (6).

For $\ell = 0$ Eq. (109) can be solved analytically. Writing out the gradients in cylindrical geometry yields

$$\frac{1}{r}\frac{\partial}{\partial r}\left(r\epsilon_{11}\frac{\partial\delta\Phi_p}{\partial r}\right) = \frac{1}{r}\frac{\partial}{\partial r}\left(r(1-\epsilon_{11})\frac{\partial\delta\Phi_{ext}}{\partial r}\right). \tag{110}$$

This equation can be integrated once. The constant of integration must be dropped to keep the potential finite at the origin, and therefore, we have

$$\frac{\partial\delta\Phi_p}{\partial r} = \frac{1-\epsilon_{11}}{\epsilon_{11}}\frac{\partial\delta\Phi_{ext}}{\partial r}. \tag{111}$$

Applying this expression to Eq. (107) and using this result in Eq. (103) yield the following expression for the acceleration admittance in cold fluid theory:

$$Y_a = \left.\frac{\omega^2(\epsilon_{11}-1)}{n(r)\epsilon_{11}}\right|_{r=r_{meas}}. \tag{112}$$

In Fig. 17, we compare the cold-fluid prediction for $Im[Y_a]$ from Eq. (112) to the numerically determined values from the Vlasov code for the standard plasma profile with $r_p = 4.76$, $r_W = 10$. There are several differences in these results compared to previous $\ell \neq 0$ results. First, for $\ell = 0$, there are no secondary Bernstein peaks within the primary admittance peak. Also, the frequency at which the single peak occurs depends on which radius it is measured at. (For global normal modes, this would not be the case.)

The cold fluid predictions give primary peaks at the same frequency locations as does the code. From Eq. (112), the peaks occur where $Re[\epsilon_{1,1}(r,\lambda)] = 0$, which explains why the frequency λ of the peak varies with radius r: in fluid theory, these peaks are local upper-hybrid oscillations excited by the forcing at the location where the upper hybrid frequency is equal to the forcing frequency. However, the code results are not as sharply peaked as the fluid theory predicts, indicating that there is some extra damping mechanism at work.

This damping mechanism becomes apparent when the perturbed density predicted by the Vlasov code is plotted versus radius. This is done in Fig. 18 for frequency $\lambda = -1$. Between the cutoff radius r_{cut} and a wave-particle resonance at $r_{wpr} > r_{cut}$, a Bernstein wave causes the density to oscillate in r, with increasing wavenumber as the wave-particle resonance is approached. This is qualitatively similar to what one would expect in WKB theory, since $X \to \infty$ at the wave-particle resonance, implying that $k \to \infty$ through Eq. (58). However, WKB theory would also predict that the wave becomes evanescent for $r > r_{wpr}$ as $Re[\epsilon_{11}]$ changes sign, but this is not what the Vlasov code shows. On the other hand, the WKB equations do not apply near the resonance, so it is perhaps unsurprising that there is a discrepancy. To our knowledge, there is currently no detailed theoretical model for the behavior of the perturbed density in a Bernstein wave near a wave-particle resonance. This problem differs from, and is more difficult than, the standard "magnetic beach"[18] absorption of cyclotron waves with nonzero wavenumber k_z along the magnetic field. For $k_z = 0$, the wave-particle resonance mechanism involves drifting cyclotron orbits in a radially nonuniform equilibrium electric field, and is consequently considerably more complex.

However, we can qualitatively understand the mode broadening and increased damping caused by this Bernstein wave. One can see in Fig. 18 that the real and imaginary parts of the oscillatory density perturbation are roughly 90° out of phase, indicating a travelling wave rather than a standing wave. The oscillating source $\delta\Phi_{ext}$ is launching a Bernstein wave perturbation that is absorbed at the wave particle resonance, sapping energy from the plasma response. This Bernstein wave does not set up a normal mode because of the absorbing "boundary condition" for the wave at the location of the wave-particle resonance. The damping caused by wave absorption at the resonance is not included in the

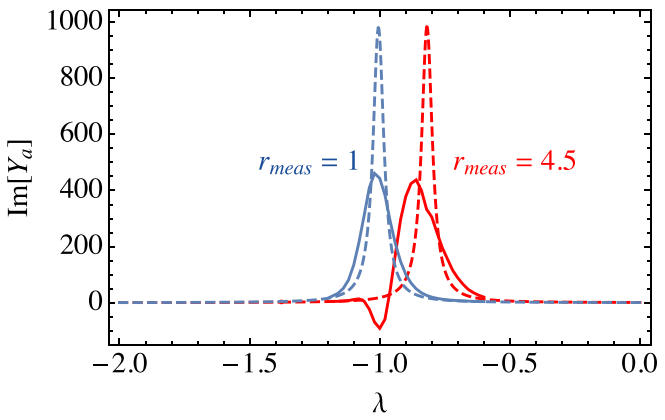

FIG. 17. Imaginary part of the acceleration admittance, measured at two radii, plotted versus scaled frequency λ for $\ell = 0$, for a plasma with $r_p = 4.76$, $r_W = 10$, and $\Omega = 5$. Dashed lines are the fluid theory prediction, Eq. (112), and solid lines are the results of the Vlasov code with $M_r = 180, M_v = 90, M_\psi = 18$.

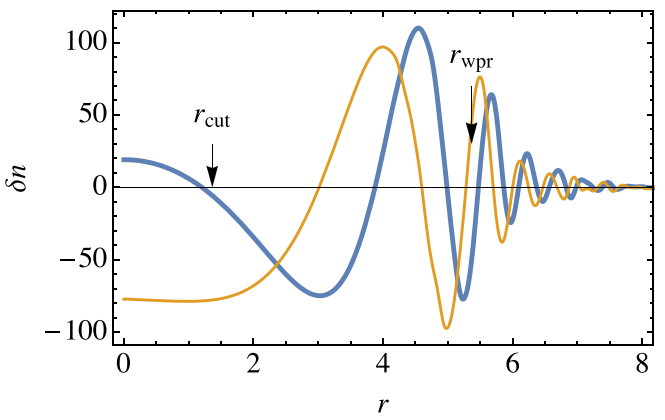

FIG. 18. Real (thick line) and imaginary (thin line) parts of the perturbed density δn versus radius, from the Vlasov code solution, for frequency $\lambda = -1$, for the same conditions as the previous figure. The small rapid oscillations on the right-hand side of the figure are not fully converged, but the oscillations near and to the left of r_{wpr} are well-converged.

cold fluid analysis (because this analysis entirely neglects Bernstein waves), and this is why the admittance peaks are sharper in cold fluid theory.

Similar enhanced damping caused by Bernstein wave absorption at a resonance was predicted via WKB analysis for $\ell \neq 0$ Bernstein waves, in Ref. 1, Sec. IX C 3. One complication in any similar WKB analysis for the $\ell = 0$ response is that the waves are now launched by a source $\delta\Phi_{ext}$ that is nonzero within the plasma. This requires a solution to the inhomogeneous wave equation, involving a WKB expression for the Green's function associated with the Bernstein mode operator; this Green's function solution was not required in Ref. 1 because there the source was a potential oscillation on the wall, outside the plasma. The WKB Green's function would produce both a fluid and a Bernstein wave response to forcing, but its functional form has not yet been derived.

We now describe the $\ell = 0$ plasma response for a second case, a plasma at lower temperature and weaker magnetic field than in the previous example: $\Omega = 1.633$, $r_p = 43.67$, and $r_W = 2r_p$. This is the case studied by Hart and Spencer. This is a plasma with a nearly uniform density and a relatively sharp edge. Figure 19 shows the result of our numerical Vlasov method for an $\ell = 0$ perturbation. There is a large peak in the admittance at $\lambda \approx -1.2$. This admittance peak is fairly well described by the cold fluid theory (the dashed line). This is an upper hybrid mode [the cold fluid admittance is peaked at the upper hybrid frequency where $Re[\epsilon_{11}] = 0$; see Eq. (112)]. However, there are also two other weaker peaks in the admittance that are not in the cold fluid theory. These peak locations in the plasma response were also observed in the simulations by Hart and Spencer (the arrows). These peaks are fairly strongly damped Bernstein modes.

In Fig. 20, we display the real and imaginary parts of the perturbed density from the Vlasov code for λ values at the three peaks. The big "cold fluid" peak is a simple "breathing mode" where the density change throughout the plasma is nearly uniform, as the plasma radially expands and compresses. There is nearly no Bernstein wave activity, which explains why cold fluid theory is a good fit to the admittance

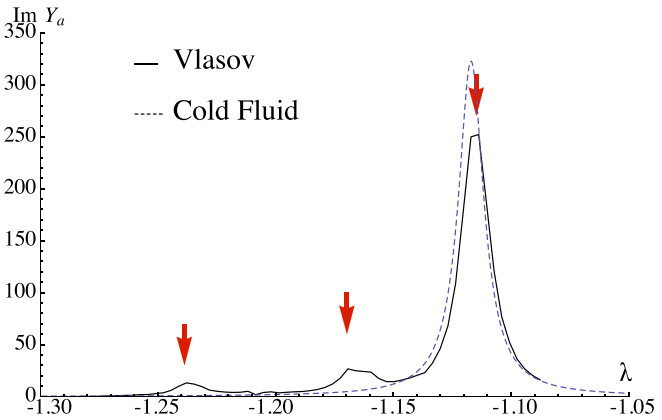

FIG. 19. Comparison of the Vlasov code, cold fluid theory, and the particle-in-cell simulation by Hart and Spencer. $\Omega = 1.633$, $r_p = 43.67$, $r_{meas} = 27.5$, $\ell = 0$, and $\nu = 1/500$. Vlasov code uses M_ψ=20, $M_r = 240, M_v = 90$. Arrows show the locations of modes found in the simulations of Ref. 6.

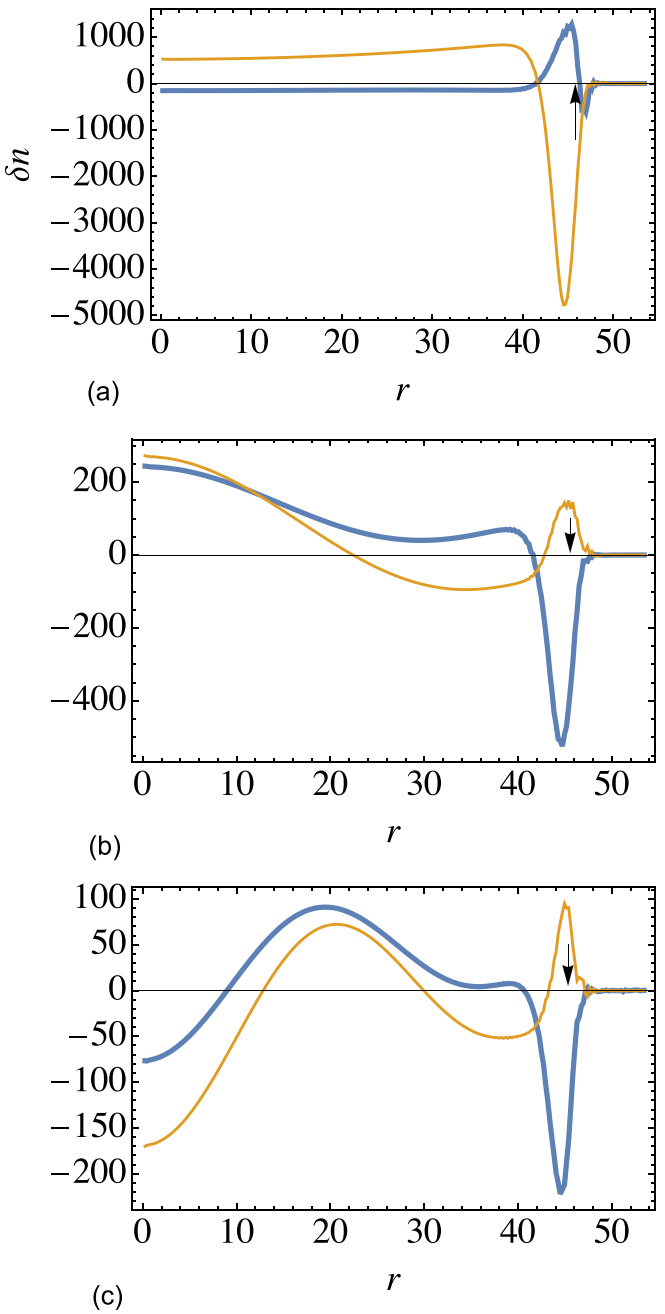

FIG. 20. Real (thick line) and imaginary (thin line) parts of the perturbed density response for $\ell = 0$ in a cold weakly magnetized plasma, at three frequencies corresponding to the peaks of the admittance in Fig. 19. (a) $\lambda = -1.11$, (b) $\lambda = -1.17$, and (c) $\lambda = -1.24$.

peak. The next two peaks show true Bernstein mode responses. The plasma density oscillates in space and the real and imaginary oscillations are not 90° out of phase; these are (damped) standing waves, not travelling waves. There is no cutoff for these modes; the Bernstein waves propagate from $r = 0$ out to a wave-particle resonance in the plasma edge (shown by the arrows). Because the wave particle resonance occurs in the plasma edge, and this edge is sharp, Bernstein waves can apparently partially reflect from the edge before they are fully absorbed at the wave-particle resonance, setting up damped normal modes.

The large variation of δn in the plasma edge exhibited in these figures is due to the "surface charge" associated with

wave motion of the sharp plasma edge. One might hope that one could model this problem using an appropriate warm fluid theory for a uniform plasma with a sharp edge, but we currently have no theoretical model for the correct wave boundary condition at this edge, since the edge both reflects and absorbs the wave due to the wave-particle resonance. Some progress has been made on this problem by treating the plasma as an elastic fluid with an anisotropic pressure tensor,[6] but this approach neglects the wave damping effect of the wave-particle resonance.

IX. CONCLUSIONS

Two electrostatic cyclotron modes propagate in a nonneutral plasma column: surface cyclotron and Bernstein waves. In this paper, we have considered the z-independent ($k_z = 0$) versions of these waves. We focussed on these z-independent waves because for $k_z \neq 0$ there can be strong Landau-damping on the parallel velocity distribution via the "magnetic beach" mechanism[18] when $(\hat{\omega} - \Omega_v)/k_z$ is of order the thermal speed v_t. Since $\hat{\omega} - \Omega_v$ is of order the plasma rotation frequency ω_r, the condition for negligible Landau damping of $k_z \neq 0$ cyclotron modes can be written as $\omega_r \gg k_z v_t$. This regime requires cold plasmas, where the Bernstein response of chief interest in this paper would be difficult to observe.

The surface wave propagates only along θ and causes density perturbations confined to the surface of the plasma. The theory of these modes is adequately described by the cold fluid theory described in Sec. III. These surface modes can be driven and detected from the wall by applying or measuring voltage on wall electrode sectors. In experiments, these modes provide diagnostics for plasma density, species concentration, and charge to mass ratio.

On the other hand, the Bernstein wave is a finite temperature effect coming from the non-zero Larmor radius of the particle orbits, introducing radial variation extending from the plasma center to the upper-hybrid radius r_{UH}, where the waves become evanescent and eventually match onto the vacuum potential outside the plasma. This is possible because the upper-hybrid radius acts as a classical turning point, where the Bernstein waves are reflected, which enables a standing wave in the interior of the plasma. In general, a plasma can have more than one upper-hybrid radius, which causes annular regions where Bernstein modes are present, where the plasma dielectric $\epsilon_{11} < 0$. We also found that for appropriate frequencies, it is possible for the plasma to have a local wave-particle resonance where the vortex frequency Ω_v matches the mode frequency as seen in the rotating frame. At radii where a resonance is present, or nearly present, the Bernstein wave energy is absorbed, making the measured wall signal significantly smaller.

Our theory began from a z-independent global thermal equilibrium density profile and determined the linear modes and mode frequencies in two different ways. First, we described and presented results from a numerical solution to the Vlasov equation; and second, we derived a new WKB theory which corrects a frequency shift in the predicted mode frequencies (predicted in the existing literature[1]) for moderately sized bare cyclotron frequency Ω. Mode frequencies were obtained and compared by picking out peaks in the admittance function $Y(\omega)$, where the mode is resonant.

The numerical solution to the Vlasov equation described in Sec. IV is valuable because it does not carry out the mathematical approximations used in the WKB theory, and therefore, the results obtained from the code are "exact" (provided the numerics have converged). These numerical results showed the surface cyclotron mode response, broadened in frequency by the variation of the $E \times B$ rotation rate across the plasma radius, as well as showing a number of individual Bernstein modes coupled to the surface cyclotron mode. We showed a number of results at various temperatures and magnetic fields, for single-species plasmas at various θ-mode numbers ℓ and then described WKB theory and presented results for plasmas with multiple species. Finally, we compared to an existing azimuthally symmetric particle-in-cell simulation and found good agreement with our Vlasov solution.

The semi-analytical WKB approach makes some simplifying assumptions, so these results were validated with the Vlasov method. In the WKB theory, the plasma was separated into four partially overlapping regions where different approximations were made. For the center of the plasma, where the plasma density is uniform, we made use of the derivation in Sec. V A giving the general form for a differential wave equation operator in a uniform, isotropic plasma. Away from the origin where the plasma density changes gradually, the Bernstein dispersion relation was used to determine the local wavenumber as a function of radius, where Bernstein waves are present. Using a 4th order wave equation valid near r_{UH}, we found that the presence of an internal Bernstein mode only couples to the surface mode through the matching conditions on the cold fluid perturbed potential $\overline{\delta\Phi}$ at r_{UH}. This matching condition is modulated by the local phase χ of the Bernstein wave, which is responsible for shifting the vacuum potential outside the plasma and ultimately changing the (normalized) electric field measured at the wall Y, which we used as a proxy for the plasma response. This new WKB theory has very good agreement with the Vlasov solution for $\Omega \geq 4\omega_p$, which was not the case for the existing WKB theory which assumed $\Omega \gg \omega_p$. We also found an approximate dispersion relation valid for strong magnetic fields and small plasma to wall radius ratio, which shows that the mode frequencies occur whenever the Bernstein wave phase χ changes by a multiple of π. We also provided a plot (Fig. 14) that predicts the frequency range in which Bernstein modes are allowed, as a function of the plasma radius scaled to the Debye length, ℓ, and the species concentration δ_β.

There are still some aspects of this problem that need to be extended or otherwise further studied. The results in this paper were focused on Bernstein modes near the cyclotron frequency Ω, but there are also modes at multiples of Ω. Both of the main methods described in this paper can be extended to consider such higher harmonic modes without trouble. Also, as we already noted, the theory described here is a 2D analysis; it assumes the axial mode number $k_z = 0$, and also that the plasma length is very long. Many experiments do not operate in this regime, so the theory may need to be extended to include finite length effects. Finally, our analysis brings up an interesting puzzle regarding the physics

occurring near a wave-particle resonant radius. In this paper, we found many circumstances under which such a resonant radius absorbs waves, attenuating Bernstein modes and leading to smaller measured Bernstein mode wall signals. On the other hand, we also reviewed an example originally considered by Hart and Spencer[6] in which the plasma edge (containing the resonant radius) instead acts as a reflector, allowing damped standing waves to be generated on the interior of the plasma. The mechanism of this reflection and absorption is not fully understood, so this question should be pursued in future work.

ACKNOWLEDGMENTS

The authors thank Professor C. F. Driscoll, Dr. F. Anderegg, and Dr. M. Affolter for useful discussions. The authors would also like to thank the San Diego Supercomputer Center for providing computing time. This work was funded by DOE Grant No. DE-SC0018236.

[1]D. H. E. Dubin, "Cyclotron waves in a non-neutral plasma column," Phys. Plasmas **20**(4), 042120 (2013).
[2]M. Affolter, F. Anderegg, D. H. E. Dubin, and C. F. Driscoll, "Cyclotron mode frequencies and resonant absorption in multi-species ion plasmas," Phys. Plasmas **22**(5), 055701 (2015).
[3]E. Sarid, F. Anderegg, and C. F. Driscoll, "Cyclotron resonance phenomena in a non-neutral multispecies ion plasma," Phys. Plasmas **2**(8), 2895–2907 (1995).
[4]R. W. Gould and M. A. LaPointe, "Cyclotron resonance phenomena in a pure electron plasma," Phys. Fluids B **4**(7), 2038–2043 (1992).
[5]R. W. Gould, "Theory of cyclotron resonance in a cylindrical non-neutral plasma," Phys. Plasmas (1994-present) **2**(5), 1404–1411 (1995).
[6]G. W. Hart and R. L. Spencer, "Properties of axisymmetric Bernstein modes in an infinite-length non-neutral plasma," Phys. Plasmas **20**(10), 102101 (2013).
[7]T. M. O'Neil and C. F. Driscoll, "Transport to thermal equilibrium of a pure electron plasma," Phys. Fluids **22**(2), 266–277 (1979).
[8]T. M. O'Neil, "Centrifugal separation of a multispecies pure ion plasma," Phys. Fluids **24**(8), 1447–1451 (1981).
[9]A. W. Trivelpiece and R. W. Gould, "Space charge waves in cylindrical plasma columns," J. Appl. Phys. **30**(11), 1784–1793 (1959).
[10]D. Schecter, D. Dubin, A. Cass, C. Driscoll, I. Lansky, and T. O'Neil, "Inviscid damping of asymmetries on a two-dimensional vortex," Phys. Fluids **12**, 2397 (2000).
[11]D. Baldwin and A. Kaufman, "Determination of the density profile in a plasma slab," Phys. Fluids **12**, 1526 (1969).
[12]D. Dubin, "Displacement eigenmodes for cold-fluid and warm-fluid magnetized plasma oscillations," Phys. Plasmas **12**, 042107 (2005).
[13]D. H. E. Dubin, *Numerical and Analytical Methods for Scientists and Engineers* (John Wiley and Sons, New York, 2003).
[14]N. G. V. Kampen, "On the theory of stationary waves in plasmas," Physica **21**, 949 (1955).
[15]R. C. Davidson, *Physics of Nonneutral Plasmas* (Imperial College Press London, 2001).
[16]H. Jeffreys, "On isotropic tensors," in *Mathematical Proceedings of the Cambridge Philosophical Society* (Cambridge University Press, 1973), Vol. 73, pp. 173–176.
[17]H. Weyl, *The Classical Groups: Their Invariants and Representations* (Princeton University Press, 2016).
[18]T. Stix, *The Theory of Plasma Waves* (McGraw-Hill, New York, 1962).